

Master thesis

**Effect of Electropulsing on the
Microstructure evolution of pearlitic
steel**

Bhowmik, Arghya

(Computational Metallurgy)

Graduate Institute of Ferrous Technology

Pohang University of Science and Technology

2009

Effect of electropulsing on the microstructure evolution of pearlitic steel
Bhowmik, Arghya

2009

Effect of Electropulsing on the Microstructure evolution of pearlitic steel

Effect of Electropulsing on the Microstructure evolution of pearlitic steel

By

Bhowmik, Arghya
(Computational Metallurgy)
Graduate Institute of Ferrous Technology
Pohang University of Science and Technology

A thesis submitted to the faculty of Pohang University of Science and Technology in partial fulfillments of the requirements for the degree of Master of Science in the Graduate Institute of Ferrous Technology (Computational Metallurgy)

Pohang, Korea
December 21th, 2009

Approved by

Prof. Bhadeshia, H.K.D.H.



Major Advisor

Prof. Qin, Rongshan



Co-Advisor

Effect of Electropulsing on the Microstructure evolution of pearlitic steel

Bhowmik, Arghya

This dissertation is submitted for the degree of Master of Science at the Graduate Institute of Ferrous Technology of Pohang University of Science and Technology. The research reported herein was approved by the committee of Thesis Appraisal

December 21th, 2009

Thesis Review Committee


Chairman: Prof. Lee, Hae Geon

(Signature) 

Member: Prof. Kim, In Gee

(Signature) 

Member: Prof. Suh, Dong Woo

(Signature) 

MFT
20080939

Bhowmik, Arghya
Effect of electropulsing on the microstructure evolution of
pearlitic steel, Department of Ferrous Technology
(Computational Metallurgy) 2009
Advisor: Prof. Bhadeshia, H.K.D.H; Prof. Qin, Rongshan Text in
English

Abstract

This work aims to model the thermodynamic impact of electropulsing. Theoretical modeling for electromagnetic and thermodynamics of electropulsing is done. Simulation study for ferrite cementite system is carried out. It suggested that electropulsing can transform cementite plates into nano sized particles at room temperature.

To prove the theory, fully pearlite steel wires are severely plastically deformed to generate non equilibrium state to promote effect of electropulsing. Afterwards, single high density pulse was used, which resulted in cementite particles in less than a millisecond time at room temperature as predicted by theoretical analysis. Afterwards, X-ray diffraction, microscopy, resistivity measurement and hardness testing is done to characterize the changes by electropulsing treatment.

This work proposes a powerful way to design and achieve normally hard to obtain microstructures by altering the thermodynamics of phase transformation by using electropulsing as done in pearlitic system.

Contents

Abstract	1
Contents	2
Nomenclature	4
Chapter 1: Introduction	
1.1: Overview	6
1.2: Literature review	
1.2.1: Effect of electropulsing on dislocation and recrystallization	7
1.2.2: Effect of electropulsing on crack healing	10
1.2.3: Effect on nucleation rate and nano structure formation	14
1.2.4: Electro plastic effect	17
1.2.5: Diffusion and precipitation enhancement	22
1.2.6: Effect on resistivity	24
1.3: Aim of work	25
Chapter 2: Theoretical analysis and simulation	
2.1: Overview	26
2.2: Electromagnetic equations	26
2.3: Finite element method	27
2.4: Finite difference method	28
2.5: Local joule heating	31
2.6: Data used for simulation	31
2.7: Uneven resistive heating pattern	32
2.8: Boundary condition for electromagnetic simulation	40
2.9: Relation to thermodynamics	41
2.10: Geometry for excess free energy calculation	44
2.11: Results for energy calculations	45
2.12: Perspective on equivalent resistivity	49

Chapter 3: Experimental procedure	
3.1: Electropulsing experiment setup	51
3.2: X-ray diffraction	57
3.3: Optical microscopy	58
3.4: Scanning electron microscopy	59
3.5: Resistivity measurement	60
3.6: Hardness test	60
Chapter 4: Experimental result and analysis	
4.1: Choice of material	62
4.2: Electropulsing	63
4.3: Optical microscopy	63
4.4: Scanning electron microscopy	66
4.5: X-ray diffraction	74
4.5.1: Alterations in peak positioning	75
4.5.2: Relation to alloying element distribution	80
4.5.3: Peak broadening factors and analysis	81
4.5.4: Cementite peaks	88
4.6: Resistivity Measurement	90
4.7: Hardness test	91
Chapter 5: Conclusion	93
References	95
Acknowledgement	103

Nomenclature

$\frac{\partial}{\partial t}$	Partial derivative with respect to time
$\frac{\partial}{\partial x}$	Partial derivative with respect to x direction
ΔG_{EM}	Change in electromagnetic free energy of the system
∇	Vector differential operator
Φ	Electric potential
Φ_i	Potential at point indexed i
λ	Wavelength
μ	Magnetic permeability
μ_0	Permeability of space
ρ	Total charge density
ρ_r	Resistivity
σ	Electric conductivity
σ_{eq}	Equivalent conductivity
σ_{rs}	Residual stress
a	area of cross section
A	Magnetic vector potential
a_α	Lattice parameter of ferrite
AC	Alternating current
b	Burger vector
B	Magnetic field
B^x	Broadening in diffraction peak
C	Capacitance
C_α	Carbon in ferrite in at %
C_i	Capacitance of capacitor i
C_{eq}	Equivalent capacitance
D	Electric displacement field
DC	Direct current
dV	Small volume element
dW	Elemental work done

E	Electric field
EM	Electromagnetic
F	Electromagnetic free energy
F_{dv}	Electromagnetic free energy of volume element dV
F_e	Force due to electric field
G	Shear modulus
H	Magnetizing field
I_{ECP}	Electropulsing current
j	Current density in a small element
j_x, j_y, j_z	X, y, z component of current
J	Total current density
J_e	Equivalent current density
J_f	Free current density
l	length
N_A	Optical aperture
$O()$	Error function
Q	Resistive heat generated
r	Position vector
r_x, r_y, r_z	X, y, z coordinate of position vector
R_i	Resistance of conducting element indexed i
SEM	Scanning electron microscope
SF	Stacking fault
t	Crystallite size
v_d	Drift velocity
V_{osc}	Voltage in the oscilloscope

Chapter 1

Introduction

1.1 Overview

Phase transition can be controlled and manipulated by the designation of environmental conditions acting upon the system. Heat treatment, particle and wave radiations, hydraulic pressure, electric and magnetic fields are some of the frequently seen methodologies that are applied in alloy processing with the aim of enabling designed phase transition. Metallic materials, such as steel and iron-alloys, gain different microstructures and hence various properties after different processing histories. Exploration of the phase transition under unusual external conditions provides not only the new opportunities for fabricating new materials, but also the scientific understanding of the material-environment interaction.

Electric current pulse (or sometimes called electropulsing) with current density above 10^9 A/m² and pulse duration in a few dozens of microsecond is one of such treatments for alternating phase transition in steels. Although the required peak current density looks high, it is easy to achieve in practice because of its fact of short duration. The principle for generating this type of electropulse is thus: a small amount of continuous power is accumulated in energy storage devices like capacitors over a relatively long period, and then released in the load system to be treated within a short time. The average power of electropulsing is defined as the total energy dissipated per second. Given the fact that majority of the time the pulsing system is getting charged and no discharge is taking place, the average power is orders of magnitude lower than the required peak pulse power during electropulsing experiment. For example, if one watt of constant power is stored for one second and then released in one microsecond, theoretically the peak energy can reach up to megawatt level. In this manner pulsed power of hundreds of terawatts can be achieved without difficulty.

There were many researches accomplished in the application of electropulsing to metallurgy. This includes the microstructure refinement, nucleation and growth control during solidification, recrystallization, crack healing etc. The previous works are reviewed in the next section. The aim of the work was to provide the new insight of electropulsing effect and explore its further application in steel processing.

1.2 Literature review

1.2.1 Effect of electropulsing on dislocation and recrystallization

Application of direct current (DC) electropulsing on cold worked copper resulted in refined microstructure [Conrad *et al.*, 1983, 1984, 1988, 1990]. This is thought due to the short treating time, high heating rate, accelerated nucleation and lower final dislocation density under electropulsing condition. The lower dislocation density in recrystallization means the lower driving force for crystal growth. Dislocation structure in electropulsed sample is found vast different from that of the thermal treated one. The movement of dislocation is enhanced by electropulsing through the mechanisms of: a) Electron wind effect; b) localized (atomic scale) heating; c) Increment of the dislocation vibration frequency, and d) improvement of sub-grain coalescence. When the dislocation density gradient is accumulated to a certain level the interior region of recrystallized nucleus formed in the lower dislocation density regions and boundaries formed in the higher dislocation density region. It is also found out that the major effect of electropulsing happens in the early stage of grain formation and not in the later grain growth stage [Conrad *et al.*, 1988]. The nucleation rate in recrystallization is proved experimentally about 10^4 times higher under electropulsing than that of without electropulsing. This is impossible to be understood by electropulsing-assistant dislocation migration theory only, and suggests further exploration of the effects of electropulsing on nucleation.

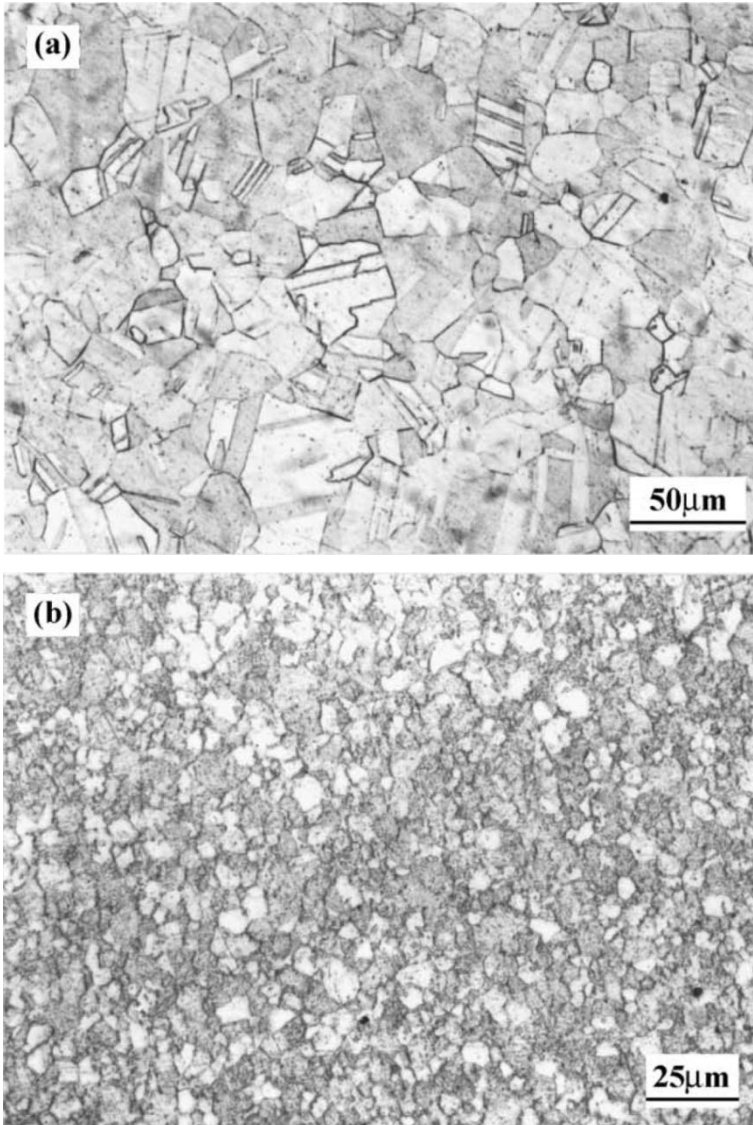
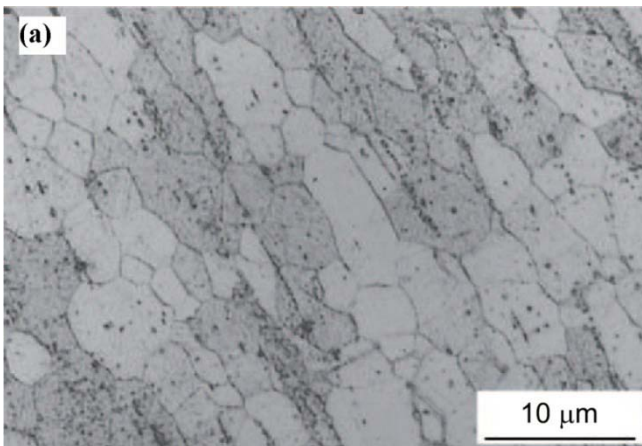


Fig. 1.1: Optical Macrograph of cold worked brass by a) annealing 650°C b) electropulsing 632°C [Zhou *et al.*, 2004]

Studies on the effect of high density electropulsing on fatigued copper single crystal found to improved sub-grain coalescence [Xiao S.H. *et al.*, 2002a, 2002b]. Thermal compressive force plays a vital role in moving dislocation along primary slip bands. The presence of more dislocations in persistent slip bands possesses higher local resistance and therefore more temperature increase under electropulsing.

This helps dislocations move to the boundary and vanish in the band. So the recrystallized grains shrunk in size and become ellipse in shape. Zhou et al performed recrystallization experiment with 67% cold worked brass [Zhou *et al.*, 2004] under electropulsing and obtained finer grain size, lower dislocation density and low twin frequency in comparison to that of experiment under thermal annealing, as is illustrated in figure 1.1.

Research on the effect of multiple electric current pulses on severe deformed (96% cold worked) low carbon steel wire gave refinement microstructure, as demonstrated in figure 1.2 [Ding F. *et al.*, 2007]. The electropulse-treated steel wire possesses much larger elongation but without much loss in tensile strength. It was suggested that the superfine grains were formed due to the higher nucleation rate and slower growth rate during the electropulsing treatment. It was also noticed that the direct current did not have any positive effect. The pulsed electric current played the role.



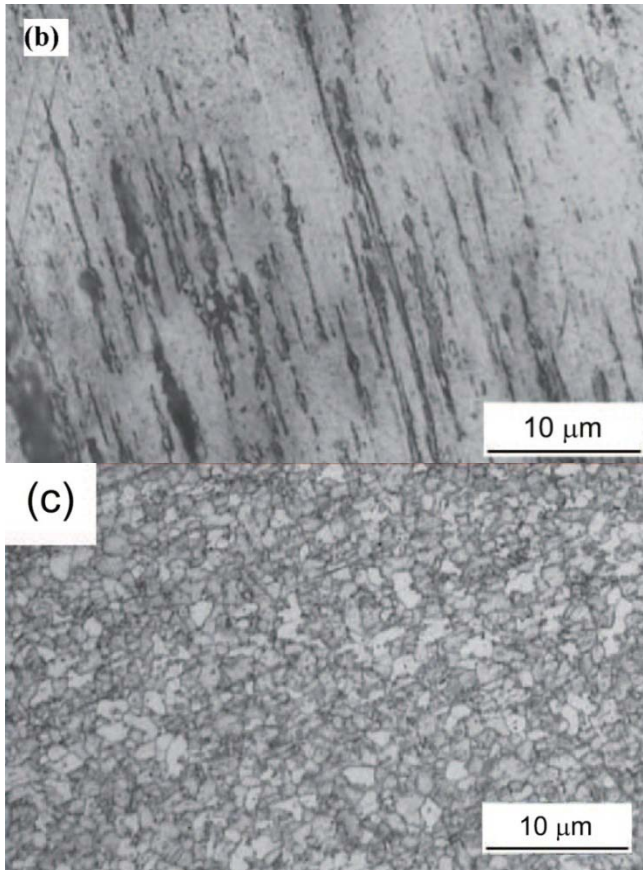


Fig. 1.2: SEM micrograph of a) commercial as annealed wire b) cold worked c) electropulse treated at 130V [Ding *et al.*, 2007]

1.2.2 Effect of electropulsing on crack healing

Experiment on 7475 aluminum alloy revealed that the voids or cavities could be healed by electric field [Conrad *et al.*, 1991]. Tang reported the improvement of surface finishing and scratches healing by electric pulse treatment [Tang *et al.*, 2000]. Yao found the electric current reduces surface micro-cracks and wearing of steel wire caused by instrument grip, as illustrated in figure 1.3, and suggested that the softening effect and the influence of drift electrons on deformation were responsible [Yao *et al.*, 2001].

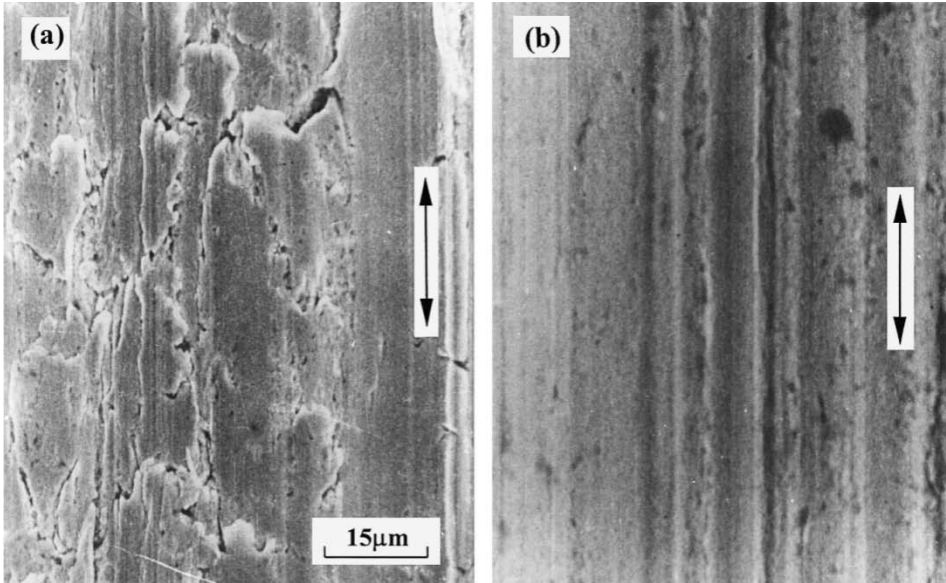


Fig. 1.3: Surface morphology of as drawn wire deformed a) without and b) with electric current treatment. Arrowhead shows drawing direction [Yao *et al.*, 2001]

A study of 1045 steel showed that electropulsing healed quench cracks [Zhou *et al.*, 2001]. It was noticed equiaxial grains of non-martensite or non-ferrite crystals with high carbon content and lower hardness in the healed area. Figure 1.4 is the SEM micrograph.

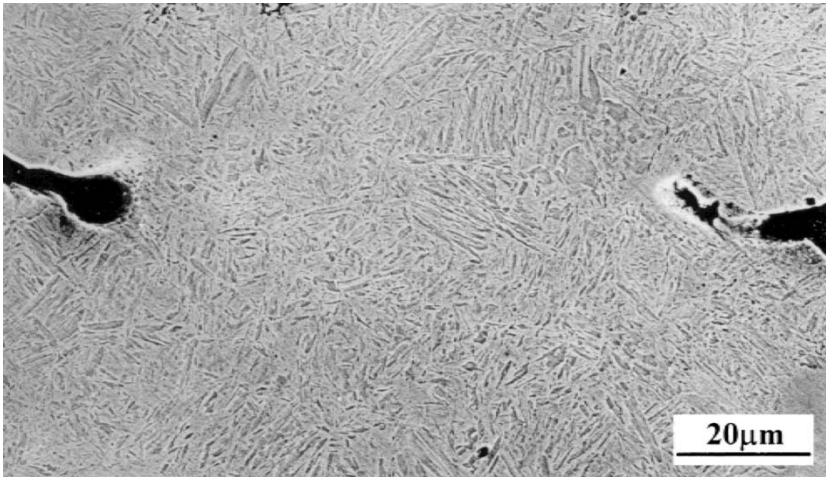


Fig. 1.4: SEM micrograph of electropulsing healed part of a crack on 1045 steel

[Zhou *et al.*, 2001]

The temperature change due to joule heating was just 200K, negating any chance of phase transition present. Three major propositions were made to explain the phenomena. The first is that the edge dislocations move into the crack. The second opinion is due to diffusion filling. This mechanism supports carbon abundance observed near the healing tip. Compression fill is another mechanism. The high thermal stress generated by asymmetric heating profile puts compressive force on the crack and decreases the distance between two sides of the crack.

Qin et al developed rigorous theory towards understanding of this phenomenon [Qin *et al.*, 2002]. The thermodynamic driving force for healing cracks was calculated and was proportional to square of current density. The current density above the critical value (30-60 A/cm² for different metals) enables to heal crack. It was also suggested that for best effect of crack healing, the electropulsing treatment should be designed such as that, the temperature raised by joule heat is lower than structural transformation temperature in the bulk material but higher than the melting temperature at the crack region so that the structural integrity is maintained but the crack closes. The temperature increment around crack is usually 20% or higher than that of in bulk, according to the numerical results by the author.

Experimental studies with mid carbon steel show that ferrite forms at the healed cracks and martensite around it [Zhou *et al.*, 2004]. This is shown in figure 1.5. They also applied electropulse to saw blade and found micro-cracks were healed and martensitic hardness were retained [Zhou *et al.*, 2003].

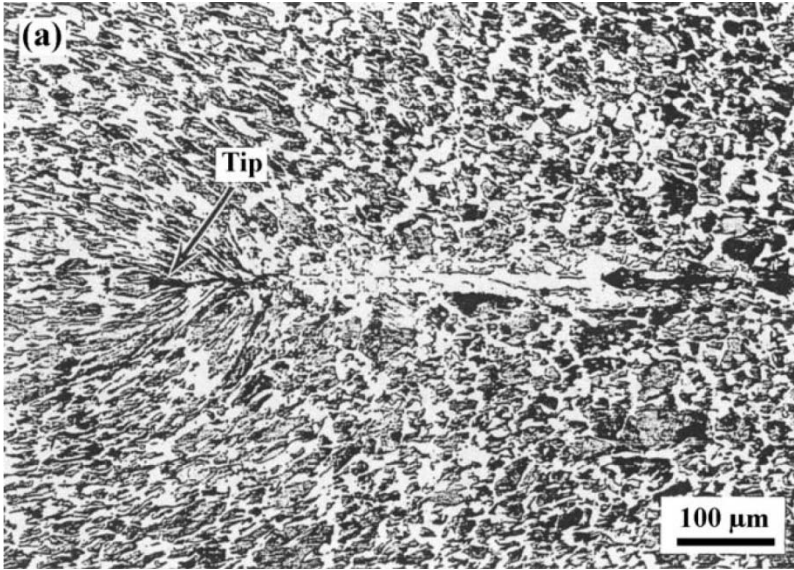


Fig. 1.5: a) Optical b) SEM micro graph of a crack partially healed by electropulsing (F=ferrite M=martensite) [Zhou *et al.*, 2004]

1.2.3 Effect on nucleation rate and nano structure formation

Conrad et al has studied the effect of electropulsing on nucleation rate since 1980s [Conrad *et al.*, 1983, 1984, 1988]. They examined the effects of frequency and duration of electropulse and concluded that the theory based on drift electron by electropulsing unable to explain the observed phenomena [Conrad *et al.*,1990]. The colony size of the cast of tin lead alloy under electropulsing is reduced in an order of magnitude. It was suggested that the electric current might affect nucleation barrier. Due to the lacking of understanding, no direct relationship was established [Barnaket *al.*, 1995].

The quantitative relationship between nucleation rate and applied electropulsing parameters was developed latterly [Qin *et al.*, 1998]. They calculated the excess free energy due to current distribution for a spherical nucleus and found that the thermodynamic barrier for nucleation was enhanced if the new phase possessed higher conductivity. Higher nucleation rate causes smaller grain size in casts. It was found that even current density of 10^3 A/cm^2 could produce an order of magnitude decrease in grain size, which addressed the questions found experimentally by previous researchers. The paper neglected the effects of pinch force and joule heating, which might become important in the cases of extremely high electric current density or longer pulse duration. Similar work on the growth rate of a nanocrystalline from amorphous alloy shows that, depends upon the resistivities of the amorphous and crystalline phases, electropulsing can retard or even stop the nanocrystalline growth. For Ni80-P20 alloys, the critical current density to suspend the growth of a 13 nm crystal from its amorphous state is around $2.56\text{-}2.59 \times 10^3 \text{ A/cm}^2$ [Qin *et al.*, 1998b].

Zhang et al observed some nano grains after electropulsing coarse-grained Cu-Zn alloy and deduced that it was due to local overheating and then fast cooling [Zhang *et al.*, 2000]. If the local heating is the only action that current pulses have then laser pulses should have similar effect as electropulsing treatment. This was proven wrong later [Zhou *et al.*, 2004].

Chinese scientists also studied the effect of high current density electropulsing on microstructures of steel and other materials [Zhou *et al.*, 2002, 2002b, 2002c; Zhang *et al.*, 2002]. Tremendous changes happened in microstructure of low carbon steel due to even a single pulse treatment. At current density up to 10.5 kA/mm^2 and pulse duration $130\mu\text{s}$, they reported the dramatic result in steel, as illustrated in figure 1.6 [Zhou *et al.*, 2002].

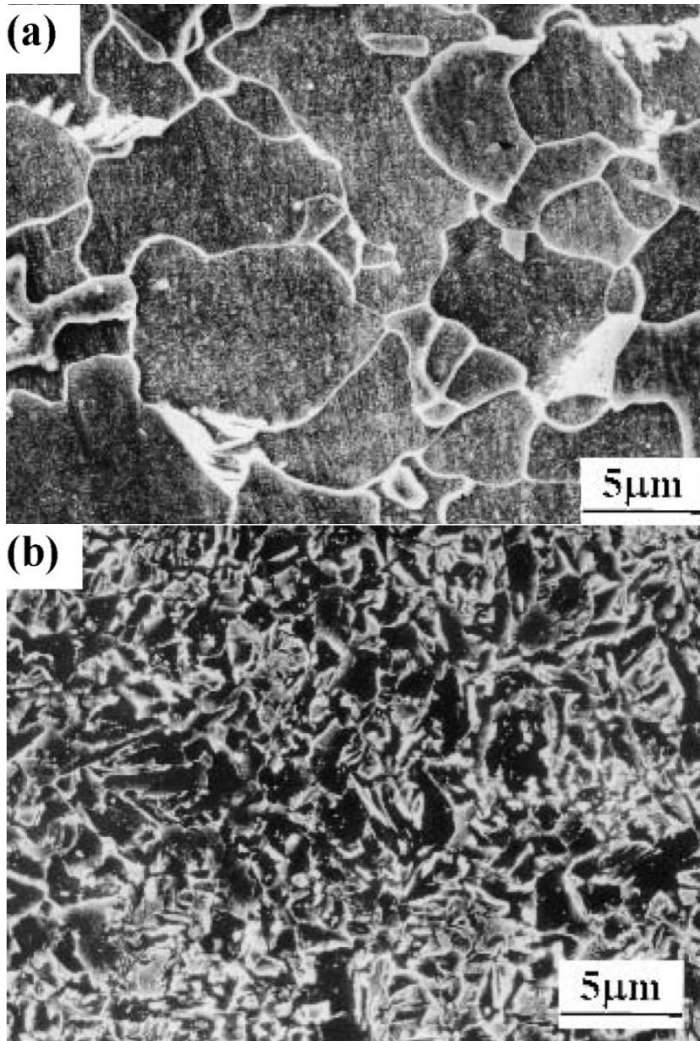


Fig. 1.6: SEM micro graph of annealed sample a) without current b) current density 10.5 kA/mm^2 ; pulse duration $130\mu\text{s}$ [Zhou *et al.*, 2002]

The transformation of coarse grained α -Fe into many nanostructured γ -Fe (5-10 % volume fraction) with grain size as small as 10nm was reported by the same group. During phase transformation austenite formed from pearlite regions could not transform back due to high alloying element content and very fast transformation time as this reaction is diffusion controlled and slow. Austenite is stabilized by electric current and forms this nanostructure. Further experiments showed grain size reduction of order of magnitude happens in 0.07% carbon steel undergoing $\alpha \rightarrow \gamma \rightarrow \alpha$ change on application of high density electropulsing.

Comparison of electropulsing treatment, laser treatment (10^6 K/s) along with normal heat treatment on Cu-Zn alloy proved that electropulsing definitely enhances nucleation during phase transformation whereas laser heating do not have an extra advantage over normal heat treatment in terms of microstructure development. No nanocrystallites have been produced by laser treatment of steel. The extreme high heating rate does have some good effects but primarily it is the thermodynamic effect of electric current that helps to reach the microstructure obtained during experiments. It is expected that, because higher conductivity of γ phase, the nucleation rate of austenite grains were much higher during 1st phase transformation, allowing very small austenite grains to form. When 2nd phase transformation to α phase happens, the high volume fraction of grain boundary causes high nucleation of α phase and hence the ultrafine microstructure. To our knowledge, this explanation is questionable because austenite does not possess higher conductivity than ferrite. The ultrafine microstructure formation was found also in electropulsing of Cu-Zn alloy [Zhou *et al.*, 2003b]. Among non steel alloys, LC6 superdralumin also produces nanoscale grains of α -Al with random orientation when subjected to high density electropulsing [Zhang *et al.*, 2002]. Mechanism of formation of FCC grains with just over 100 K increase in temperature could not be satisfactorily explained or speculated by electron wind or joule heating concept.

Application of electropulsing with current density up to the order of 10^{10} A/m² to a variety of metallic alloys was experimented as well. Cold worked H62 Cu-Zn alloy shows the microstructure with randomly oriented grains of three orders of

magnitude smaller in size after electropulsing than its original. The nanostructured TiC forms in sintered TiC/NiCr cement after electropulsing however has almost same orientation. It is to be remembered that there was no phase transition in TiC and the regular orientation happened from heavy impact stress (generated from non equilibrium thermal expansion and pinch force) over its yield strength. TiC single crystals broken into nanostructured TiC grains with small mis-orientation angle and large amount of micro defects. ECP did change the defect structure as well. H62 generated a lot of sub micron twins and stacking fault due to its low SF energy (7 mJ/m²). NiCr shows twin structures even though it has very high SF energy (250 mJ/m²). So it was concluded that those twins are deformation twin not growth twin. But the thermal stress developed in superdralumin being much lower, no twins could not be formed in α -Al nanocrystallites (SF energy 200 mJ/m²).

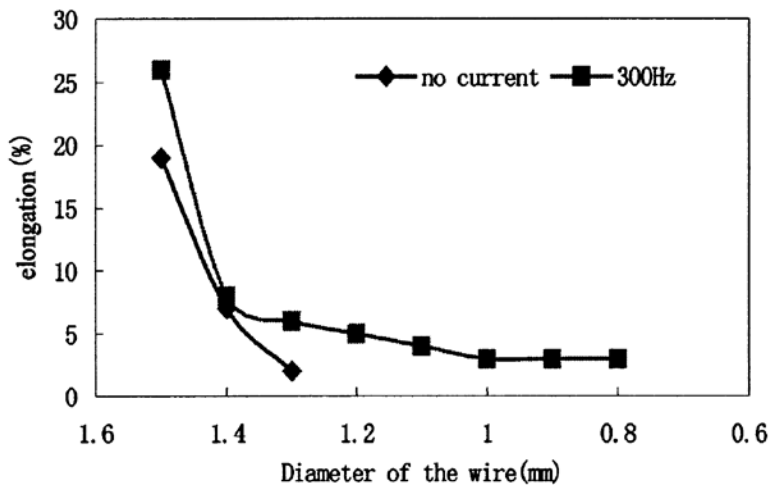
1.2.4 Electro plastic effect

One of the most studied effects of electric current on metals is electro plastic effect. It is well established that the electric current flow reduces deformation resistance, decreases strain hardening and increases plasticity. Although the ultimate tensile strength decreases significantly, there is tremendous improvement in ductility and deformation ability.

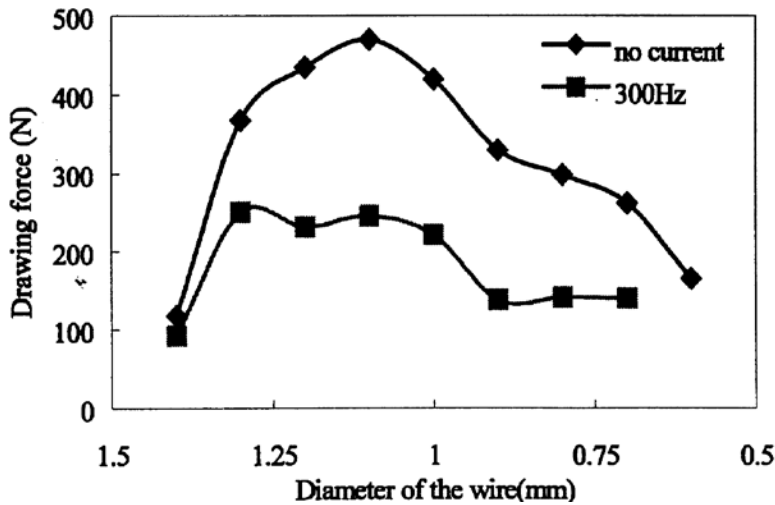
Troitskii and his group made some detailed experiments with zinc, lead, cadmium, copper, stainless steel, indium etc, under electropulse of 10³A/mm² and 50 μ s, and concluded that dislocation movement was accelerated by the drifting electrons [Troitskii,1984a,1984b; Kiryanchevet *al.*,1985; Troitskii *et al.*,1985;Troitskii *et al.*,1986; Moiseenkoet *al.*,1987]. He used electron wind and pinch force to explain the linear (lower current density) and quadratic relation (higher current density) relationships between current density and plasticity, respectively. There are a few discrepancies in his theory. For example, instead of hole mobility being higher than electron mobility, as he assumed, the opposite is found for metals like austenitic steel.

Later Conrad et al conducted massive amount of experiments in a large range of metallic materials for understanding electro plasticity and other effects of electric current on metals [Conrad *et al.*, 1983, 1984, 1988, 1989, 1989b;Cao*etal.*1989]. Although most electric field treatment experiments showed softening behavior with reduced flow stress, electric field experiment with Zn 5wt%-Al alloy showed decreased creep rate, increased strain hardening rate and strengthening of the alloy [Li *et al.*,1998] on using 3.2 kV/cm electric field during super plastic deformation testing. The effect of electric field on grain boundary sliding phenomena was also somewhat peculiar. They also found that high electric field improved the harden ability of steel during quench casting, and reduced defects and micro twins in the lathe martensite in 4340 steel (Cao *et al.*, 1990).

Electro plastic experiment on Cr18Ni9 austenitic steel showed 20%-50% and 13-34% decreases in ultimate tensile strength on application of electropulsing but, a huge improvement on elongation [Tang *et al.*,1998]. Their experiment on 304L stainless steel wire produced the similar result [Tang *et al.*, 2000]. Excess energy that provided activation energy for dislocations to overcome obstacles was accounted for the reduction of internal friction resistance.



(a)

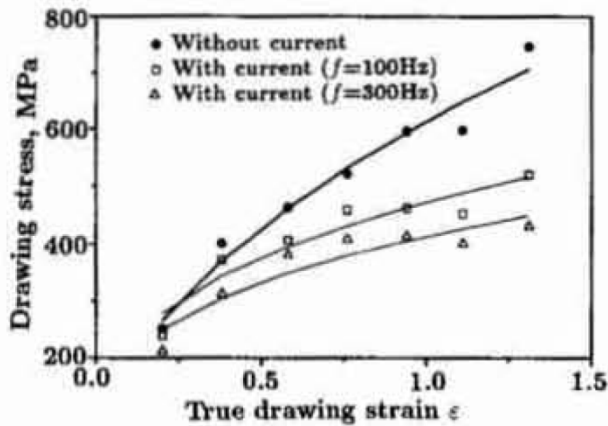


(b)

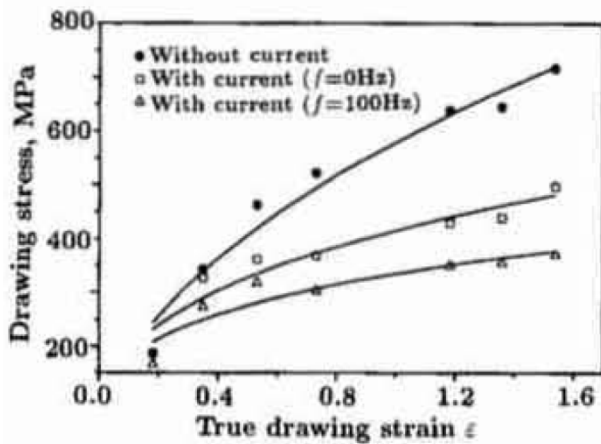
Fig. 1.7: a) Increase in elongation b) decrease in drawing force on application of 10^3 Amp/mm² 20 μ s pulse [Tang *et al.*, 2000]

Electro plasticity experiment in silicon steel correlated that the hardness decreased linearly with increasing current density [Livesey *et al.*, 2001]. Taking note of the fact that the effect was more prominent when a particular frequency was used, Tang *et al* proposed a different theoretical explanation for electro plasticity. They suggested that when the frequency of the input pulses approaches that of the substance wave in the material, there will be intensive elastic vibration of waves with the same frequency, which enables the movement of the dislocations in the material along the flowing direction with a high speed. However this explanation is flawed as the atomic vibration frequency is in much higher order than the pulse frequency.

More research on electro plasticity was done in stainless steel wire [Yao *et al.*, 2001a, 2001b]. A drop of 33% (H0Cr17Ni6Mn3), 44 % (Fe-18Cr-10Ni-.1C) and 47 % (1Cr18Ni9) of work hardening exponent, respectively, was noticed as can be seen in figure 1.8.



(a)



(b)

Fig. 1.8: Change in true drawing stress vs. drawing strain on application of electric current on a) H0Cr17Ni6Mn3 b) 1Cr18Ni9 stainless steel wire [Yao *et al.* 2001b]

Yao et al could not provide with any proper explanation. However, the drift electron causing lowering of dislocation movement barrier got some support as the effect was lower in Mn containing alloy. Manganese is known to increase resistance to dislocation movement. Opposite behavior was observed by Conrad et al a few years back on doing electropulsing on Ti-Al alloy [Yang *et al.*, 2001] Which shows increase in strain hardening and higher yield stress (similar result as application of electric field while stress testing).

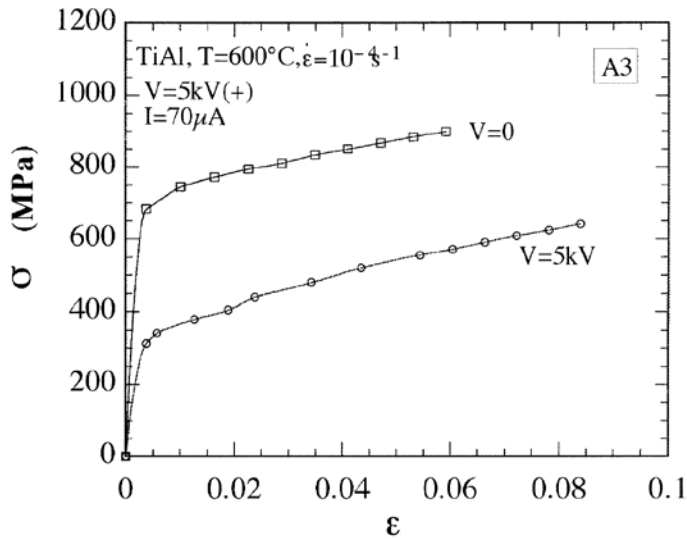
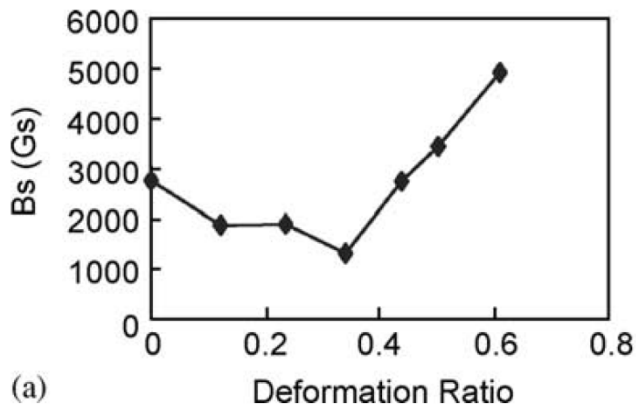


Fig. 1.9: Unexpected increase in stress level (σ) for similar strain (ϵ) during drawing of Ti-Al rod on electropulsing [Yang *et al.* 2001]

While studying electro plastic effect in cold drawing Cr18Ni9 austenitic stainless steel wire, along with expected drop in drawing stress, it was also noticed that the saturated magnetization decreases drastically. It shows that current pulses retard the formation of martensite which is ferromagnetic phase [Tang *et al.*, 2003].



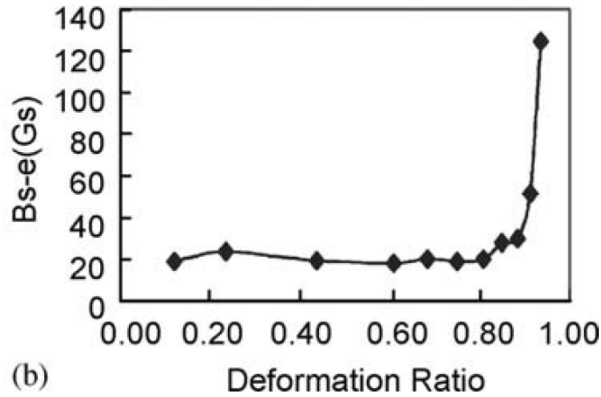


Fig. 1.10: The magnetic properties of the wire: (a) in the conventional drawing process; (b) when drawing with current pulses [Tang *et al.*, 2003].

ECP during manufacturing process is beneficial. If electropulsing is done after equal channel angular pressing, the yield stress and the ultimate tensile strength hardly decrease, but the elongation-to-failure increases to about 57% (Du *et al.*, 2008).

1.2.5 Diffusion and precipitation enhancement

Interestingly it was found that quench aging of low carbon steel was tremendously affected by electric pulse treatment. AC current of 1000 A/cm² at 100Hz appreciably reduces the age hardening behavior. With precise frequency control it is possible to completely suppress the carbon precipitation [Campbell *et al.*, 1994]. This phenomena is attributed to the fact that, when the frequency of the pulsed current was matching the carbon atom jump frequency towards vacancy site, precipitate nucleation in the BCC iron was under scrutiny. It was also concluded that electric field helps in segregation of impurity atoms at the grain boundaries [Li *et al.*, 1998].

While studying ultrafine microstructure formation in Cu-Zn by electropulsing, Zhou et al (25) noticed that electric current improved long range diffusion by a great

margin during β phase precipitation. Classical electro migration theory failed to explain the order of increased diffusion rate that is needed for supporting the formation of microstructure obtained experimentally [Zhou *et al.*, 2004]. Proposition were made that dramatic increment in diffusion coefficient and decrease in activation energy might have caused this. But no proper explanation exists.

When Fe-0.6C-1Mn-2Si steel is subjected to multi cyclic fatigue tests and then electric current is used on it, a number of phenomena happen [Sosnin *et al.*, 2005]. Carbon atoms transferred from dislocations and other structural defects and formed new globular carbide particle of ~50nm size.

If the conductivity of new precipitate is higher, then the free energy change due to electric current during the formation of this precipitate is negative, the nucleation rate of precipitate increases. On the other way if the precipitate has higher resistivity, to lower the energy of the system, inclusion dissolves and atoms are transferred to defects and grain boundary. Experimental verification of this effect with dispersion of Pb inclusions in Cu-Zn alloy on electropulsing has been performed [Wang *et al.*, 2006].

Similar phenomena happen when electropulsing annealing is done on graphite iron [Li *et al.*, 2009]. Graphite being better conductor than cementite, formation of new graphite nucleus by carbon shift from cementite is energetically favorable in the electric carrying system. The diffusivity of carbon atom also increases due to the electron wind effect, which helps in lowering incubation time. Cementite phase due to its high resistivity tends to get hotter than graphite phase. As the dislocations migrates quick at higher temperature area. This accumulates more dislocations around cementite phase, ultimately allowing it to disintegrate faster with higher carbon diffusivity (dependent temperature again). This way there is more graphite inclusions in electropulse annealed sample that thermal annealed sample, as can be seen in figure 1.11.

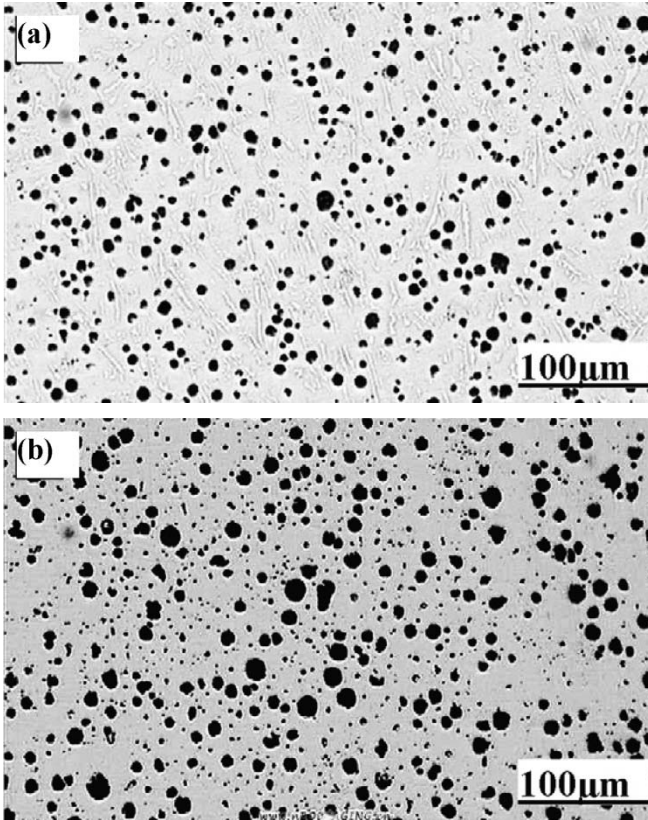


Fig. 1.11: Higher solid state solid-state graphitization of graphite iron by b) electropulsing annealing than a) thermal annealing [Li *et al.*, 2009].

1.2.6 Effect on resistivity

During electro plasticity experiment on 304L stainless steel wire, Tung noticed 10% drops in resistivity of the sample on electropulsing. This is demonstrated in figure 1.12.

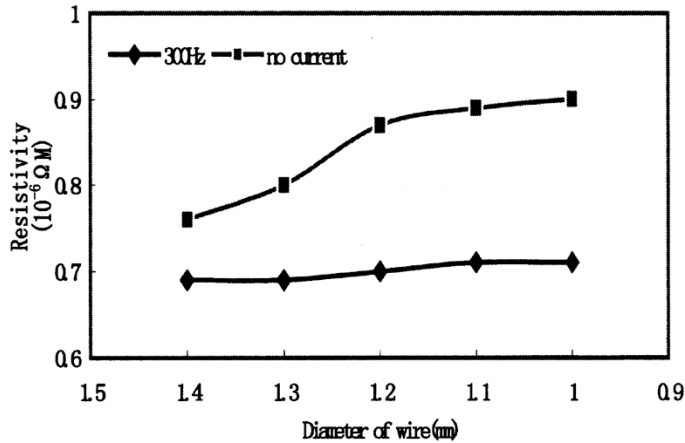


Fig. 1.12: resistivity of steel wire drops on electropulsing treatment [Tang *et al.*, 2000]

1.3 Aim of work

Out of many different outcomes of electropulsing, one of the most promising areas is the microstructure refinement. The traditional microstructure refinement methods that applied in steel industry are complicated and time consuming. Electropulsing can provide the similar refinement effect but with much short duration, low energy consumption, and low temperature processing environment. The effect of electropulsing on solid phase transformation is the focus of this work. It is designed to put together theoretical investigation, numerical calculation and experiments to tackle this problem. The ultimate target is to have clear understanding of the phase transition in current carrying system, and to implement this technique in steel processing.

Chapter 2

Theoretical Analysis and Simulation

2.1 Overview

To promote phase transformation in a system, which is otherwise not possible, electropulsing must make it thermodynamically favorable. This means, the way electricity flows around in the material must have some link to the thermodynamic stability of the material. So the primary goal is to find out the relation of electricity distribution to thermodynamics of the system, and then to correlate any microstructural change to it.

Consider a current carrying system consisting of a homogeneous single phase; the current density will be uniform everywhere. If by any means new phase is formed, heterogeneity in current flow happens. Then again if conductivity of existing phases change (for example by introduction of defects [Barghout *et al.*, 1996; Dexter, 1952] or by structural relaxation [Alia *et al.*, 1982; Kelton *et al.*, 1984]) or their volume fraction changes or even the pattern of distribution (both size and geometry) of phases (microstructure of the material defines this) change, electric current will redistribute again. To have exact view of this, electromagnetic equations must be solved.

2.2 Electromagnetic equations

Two of Maxwell's equations for electromagnetism namely Ampere's law (2.1) and Gauss's law lead to the continuity of current flow equation which is used here.

$$\nabla \times \mathbf{H} = \mathbf{J} + \frac{\partial \mathbf{D}}{\partial t} \quad (2.1)$$

Applying divergence operator on both sides,

$$\nabla \cdot \nabla \times \mathbf{H} = \nabla \cdot \mathbf{J} + \frac{\partial \nabla \cdot \mathbf{D}}{\partial t} \quad (2.2)$$

As divergence of curl is zero,

$$\nabla \cdot \mathbf{J} + \frac{\partial \nabla \cdot \mathbf{D}}{\partial t} = 0 \quad (2.3)$$

From Gauss's law

$$\nabla \cdot \mathbf{D} = \rho \quad (2.4)$$

From (2.3) and (2.4)

$$\nabla \cdot \mathbf{J} + \frac{\partial \rho}{\partial t} = 0 \quad (2.5)$$

Now for a steady state conductivity problem we can simplify it as

$$\nabla \cdot \mathbf{J} = 0 \quad (2.6)$$

As current density is proportional to electric field

$$\mathbf{J} = \sigma \mathbf{E} \quad (2.7)$$

Relation between electric field and electric potential

$$\mathbf{E} = -\nabla \Phi \quad (2.8)$$

Substituting J in (2.6) by equation (2.7)

$$\nabla \cdot (\sigma \mathbf{E}) = 0 \quad (2.9)$$

Using equation (2.8)

$$\sigma \nabla^2 \Phi = 0$$

This is a standard partial differential equation of Laplace form.

So the main goal is to solve this equation to get potential distribution and then to obtain the current distribution by equation (2.7) and (2.8). As the potential distribution is a continuous function even across boundaries, it will enable us to use numerical solution methods.

Numerical solution of Laplace equation can be done both by finite element method and by finite difference method.

2.3 Finite element method

To solve the differential equation numerically, first the boundary of the domain, for which the solution has to be done, is approximated by polygons. Then the domain is

divided into small elements. This procedure is called meshing. Then linear functions are derived from the PDE to be solved and applied to each element and vertices to ultimately generate solution. This allows treating even intricate geometry and also having higher level of accuracy than finite difference method. Standardized FEM solver is used in this work to solve different systems with appropriate boundary condition.

2.4 Finite difference method

In finite difference method we replace derivative operators in Laplace equation with discrete approximation and then use explicit iterative technique to obtain approximate solution to the equation. The typical procedure is as follows.

Let us consider three points along x-axis differentiated by a distance h labeled as $i-1$, i and $i+1$ with associated potential of Φ_{i-1} , Φ_i and Φ_{i+1} . So Taylor expansion formula is used for the two extreme points

$$\Phi_{i-1} = \Phi_i - h \frac{\partial \Phi}{\partial x} \Big|_i + \frac{h^2}{2!} \frac{\partial^2 \Phi}{\partial x^2} \Big|_i - \frac{h^3}{3!} \frac{\partial^3 \Phi}{\partial x^3} \Big|_i + \frac{h^4}{4!} \frac{\partial^4 \Phi}{\partial x^4} \Big|_i + O(h^5) \quad (2.10)$$

$$\Phi_{i+1} = \Phi_i + h \frac{\partial \Phi}{\partial x} \Big|_i + \frac{h^2}{2!} \frac{\partial^2 \Phi}{\partial x^2} \Big|_i + \frac{h^3}{3!} \frac{\partial^3 \Phi}{\partial x^3} \Big|_i + \frac{h^4}{4!} \frac{\partial^4 \Phi}{\partial x^4} \Big|_i + O(h^5) \quad (2.11)$$

Adding both of them

$$\Phi_{i-1} + \Phi_{i+1} = 2\Phi_i + h^2 \frac{\partial^2 \Phi}{\partial x^2} \Big|_i + \frac{h^4}{12} \frac{\partial^4 \Phi}{\partial x^4} \Big|_i + O(h^5) \quad (2.12)$$

$$\text{Or, } \Phi_{i-1} + \Phi_{i+1} - 2\Phi_i = h^2 \left(\frac{\partial^2 \Phi}{\partial x^2} \Big|_i + \frac{h^2}{12} \frac{\partial^4 \Phi}{\partial x^4} \Big|_i + O(h^5) \right)$$

$$\text{Or, } \Phi_{i-1} + \Phi_{i+1} - 2\Phi_i = h^2 \left(\frac{\partial^2 \Phi}{\partial x^2} \Big|_i + O(h^3) \right)$$

$$\text{Or, } \frac{\partial^2 \Phi}{\partial x^2} \Big|_i = \frac{\Phi_{i-1} + \Phi_{i+1} - 2\Phi_i}{h^2} + O(h^2) \quad (2.13)$$

Now subtracting equation (2.10) from equation (2.11)

$$\Phi_{i+1} - \Phi_{i-1} = 2h \frac{\partial \Phi}{\partial x} \Big|_i + \frac{h^3}{3} \frac{\partial^3 \Phi}{\partial x^3} \Big|_i + O(h^5) \quad (2.14)$$

$$\text{Or, } \Phi_{i+1} - \Phi_{i-1} = 2h \left(\frac{\partial \Phi}{\partial x} \Big|_i + \frac{h^2}{6} \frac{\partial^3 \Phi}{\partial x^3} \Big|_i + O(h^4) \right)$$

$$\text{Or, } \frac{\partial \Phi}{\partial x} \Big|_i = \frac{\Phi_{i+1} - \Phi_{i-1}}{2h} + O(h^2) \quad (2.15)$$

Both (2.13) and (2.15) are 2nd order approximations for corresponding derivatives.

Similar analysis along y-axis taking point j-1, j and j+1 gives us results

$$\frac{\partial^2 \Phi}{\partial y^2} \Big|_j = \frac{\Phi_{j-1} + \Phi_{j+1} - 2\Phi_j}{h^2} + O(h^2) \quad (2.16)$$

$$\frac{\partial \Phi}{\partial y} \Big|_j = \frac{\Phi_{j+1} - \Phi_{j-1}}{2h} + O(h^2) \quad (2.17)$$

These two set of equations can be superimposed for a two dimensional scheme. So a two dimensional Laplace equation in a uniform material directly transforms into

$$\begin{aligned} \nabla^2 \Phi &= \left(\frac{\partial^2 \Phi}{\partial x^2} + \frac{\partial^2 \Phi}{\partial y^2} \right) \Big|_{i,j} \\ &= \frac{\Phi_{i-1,j} + \Phi_{i+1,j} - 2\Phi_{i,j}}{h^2} + \frac{\Phi_{i,j-1} + \Phi_{i,j+1} - 2\Phi_{i,j}}{h^2} + O(h^2) = 0 \end{aligned}$$

For a stable solution eliminating the error factor

$$\text{Or, } \Phi_{i-1,j} + \Phi_{i+1,j} - 2\Phi_{i,j} + \Phi_{i,j-1} + \Phi_{i,j+1} - 2\Phi_{i,j} = 0$$

$$\text{Or, } \Phi_{i,j} = \frac{1}{4} (\Phi_{i+1,j} + \Phi_{i-1,j} + \Phi_{i,j+1} + \Phi_{i,j-1}) \quad (2.18)$$

This can also be obtained from basic understanding of Kirchhoff's laws. All the five points are taken as before and all connecting resistances (R) as same. Kirchhoff current law states that sum of all current flow at a node point should be zero which is true here as there is no built up of charge here.

$$\text{So, } \frac{\Phi_{i,j+1} - \Phi_{i,j}}{R} + \frac{\Phi_{i,j-1} - \Phi_{i,j}}{R} + \frac{\Phi_{i+1,j} - \Phi_{i,j}}{R} + \frac{\Phi_{i-1,j} - \Phi_{i,j}}{R} = 0 \quad (2.19)$$

$$\text{Or, } \Phi_{i,j} = \frac{1}{4}(\Phi_{i+1,j} + \Phi_{i-1,j} + \Phi_{i,j+1} + \Phi_{i,j-1})$$

In a system consisting of different materials, this equation does not hold good automatically. In case any the points are not in the same conductivity region, an adjustment of the weights (R) has to be performed.

If the adjacent points have different conductivities, the connecting weight should be such a function of their conductivities that the current flow must remain unchanged.

This assumption translated in to the condition,

$$\frac{1}{\sigma_{eq}} = R_{eq} = R_1 + R_2 = \frac{h_1}{\sigma_1} + \frac{h_2}{\sigma_2} \quad (2.20)$$

If h_1 and h_2 are same approximately then

$$\frac{1}{\sigma_{eq}} = \frac{1}{\sigma_1} + \frac{1}{\sigma_2} \quad (2.21)$$

Applying Kirchoff's current law again with modified weights

$$\frac{\Phi_{i,j+1} - \Phi_{i,j}}{R_1} + \frac{\Phi_{i+1,j} - \Phi_{i,j}}{R_2} + \frac{\Phi_{i,j-1} - \Phi_{i,j}}{R_3} + \frac{\Phi_{i-1,j} - \Phi_{i,j}}{R_4} = 0 \quad (2.22a)$$

$$\text{Or, } \frac{\Phi_{i,j+1}}{R_1} + \frac{\Phi_{i+1,j}}{R_2} + \frac{\Phi_{i,j-1}}{R_3} + \frac{\Phi_{i-1,j}}{R_4} = \Phi_{i,j} \left(\frac{1}{R_1} + \frac{1}{R_2} + \frac{1}{R_3} + \frac{1}{R_4} \right)$$

$$\text{Or, } \Phi_{i,j} = \frac{\frac{\Phi_{i,j+1}}{R_1} + \frac{\Phi_{i+1,j}}{R_2} + \frac{\Phi_{i,j-1}}{R_3} + \frac{\Phi_{i-1,j}}{R_4}}{\frac{1}{R_1} + \frac{1}{R_2} + \frac{1}{R_3} + \frac{1}{R_4}} \quad (2.22b)$$

This equation is primarily used in an iterative manner to reach a stable solution where the error between two steps becomes minimal.

After a satisfactory solution for potential is obtained, equations (2.15) and (2.17) are used to get electric field vector which when multiplied with conductance at a

particular point, gives the current density at that point.

2.5 Local joule heating

Once the current density at a particular point is known, resistive heating at that point can be calculated as

$$Q = \sigma \mathbf{E} \cdot \mathbf{E} \quad (4.23a)$$

$$\text{Or, } Q = \mathbf{J} \cdot \mathbf{E} \quad (4.23b)$$

This information can give valuable information about effects generated by uneven heating.

2.6 Data used for simulation

The most important material properties that are needed for simulation of pearlite microstructure carrying electricity are the resistivity of ferrite and cementite (table 2.1) and also the permittivity of pearlite

Temperature (K)	Ferrite conductivity (10^6 S/m)	Cementite conductivity (10^6 S/m)	Ratio of ferrite to cementite conductivity
293	7.02	0.93	7.55
473	3.18	0.77	4.14
683	2.43	0.68	3.57
863	1.66	0.65	2.51

Table 2.1: Linearly decreasing conductivity of ferrite and cementite over a large range of temperature within zone of thermodynamic stability.

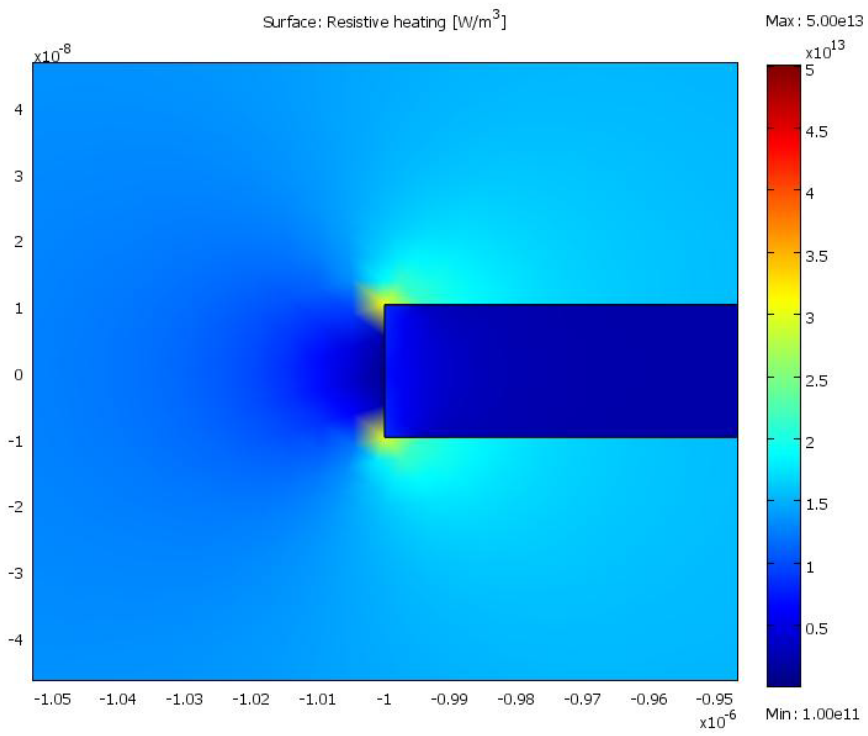
Another most important parameter, relative magnetic permeability is taken as 56 from previous work on magnetic property of pearlitic steel [Thompson *et al.*, 1994].

As spheroidization also involves structural relaxation in cold drawn pearlitic wire

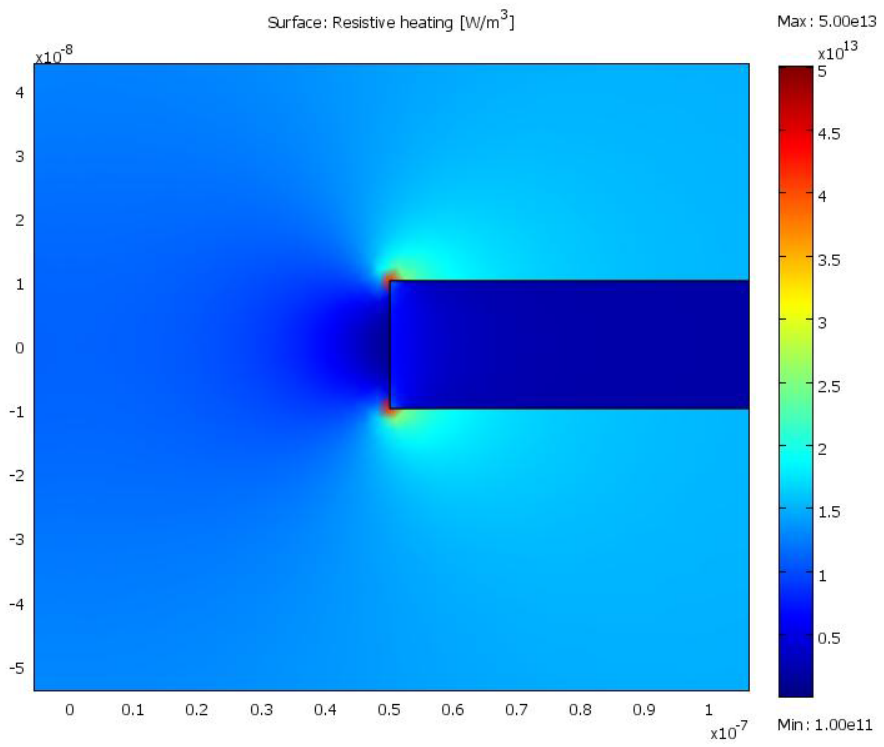
(used for experiment) which entails increment of conductivity of the phases involved, its effect will also be studied.

2.7 Uneven resistive heating pattern

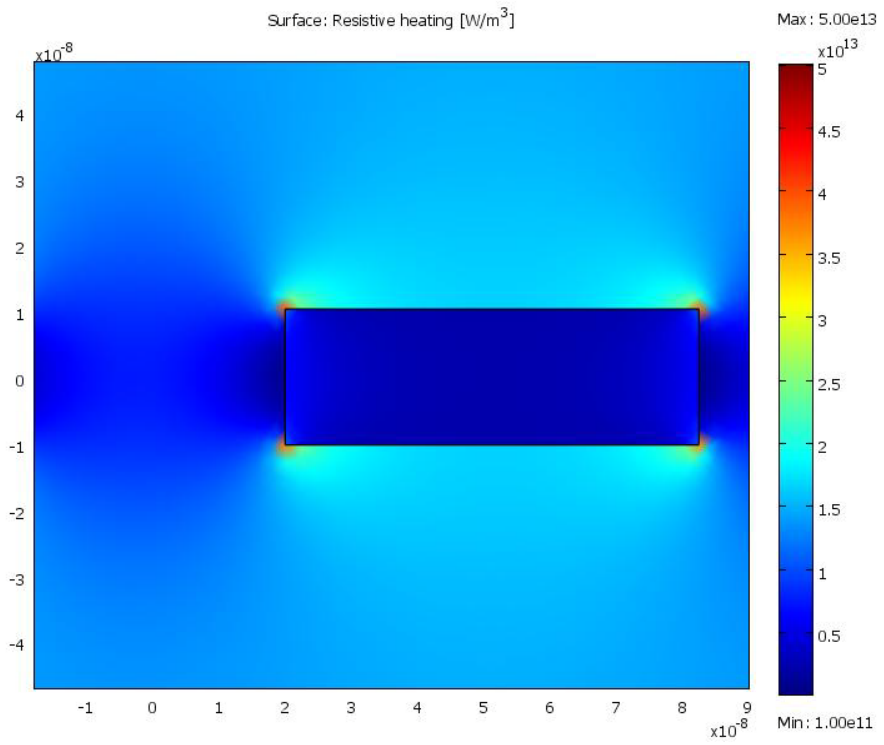
Even under the same current density, different microstructures (like those described in the last section) redistribute current differently, giving rise to different local heating pattern. Very high heating rate in a localized region compared to the surroundings, gives rise to intense pressure wave which affects phase transformation. This is evident from the simulation results in Fig. 2.1 plots. Cementite plates having higher aspect ratios of 12.5:1 and 3.125:1 have much higher contrast (smaller intense heating region) as far as heating rate is concerned though the excitation current density in the bulk is same. This should make them less stable. In the smallest particle system intense heating area is both cooler (than the partially broken geometry) and smaller (than unbroken plate)



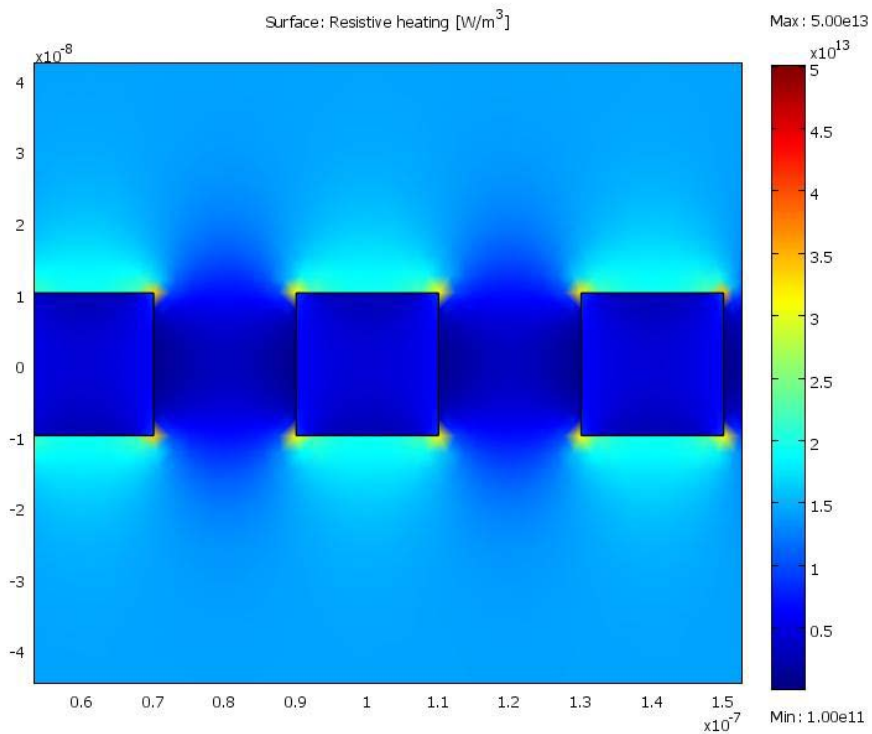
(a)



(b)



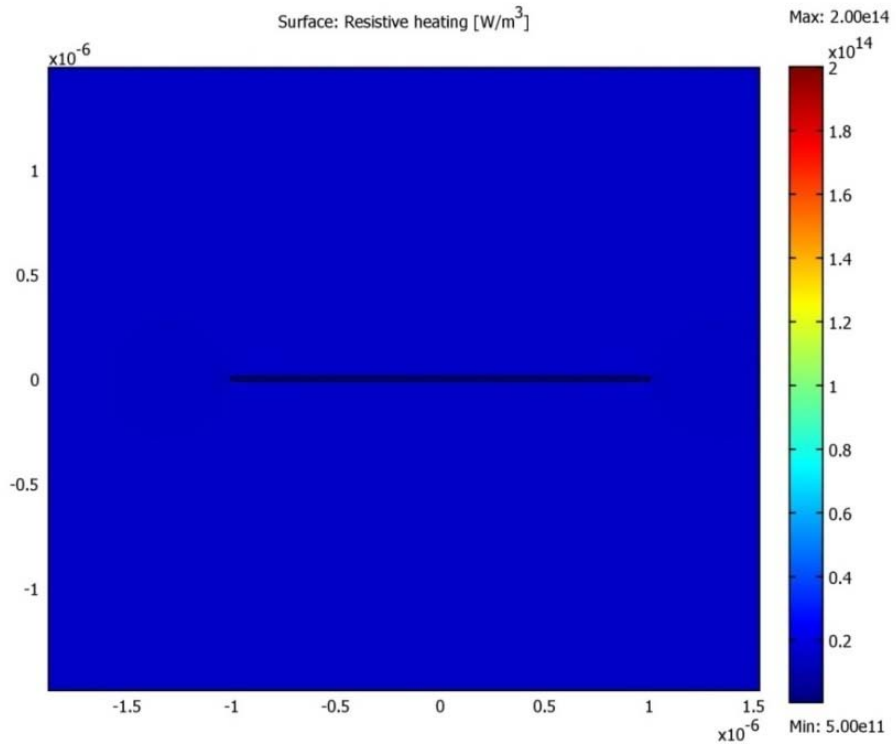
(c)



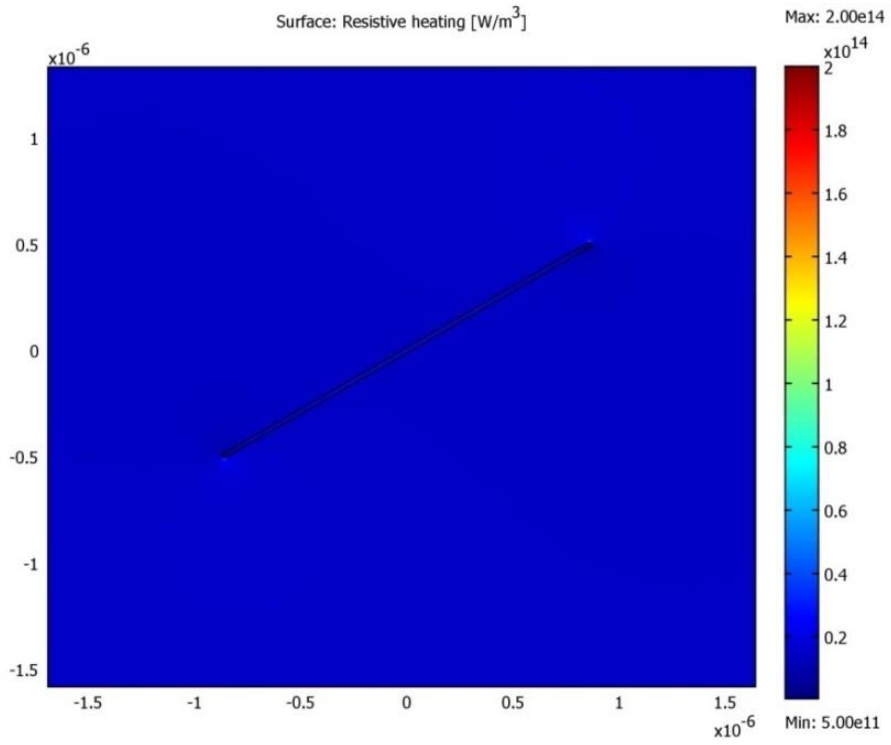
(d)

Fig 2.1: surface plot showing uneven heating pattern around cementite particle in (a) single plate (b) 8 broken 12.5:1 plates (c) 32 smaller 3.125:1 plates (d) 100 1:1 particle based simulations for matrix current density of 10^{10} A/m². (Heating scale same for all)

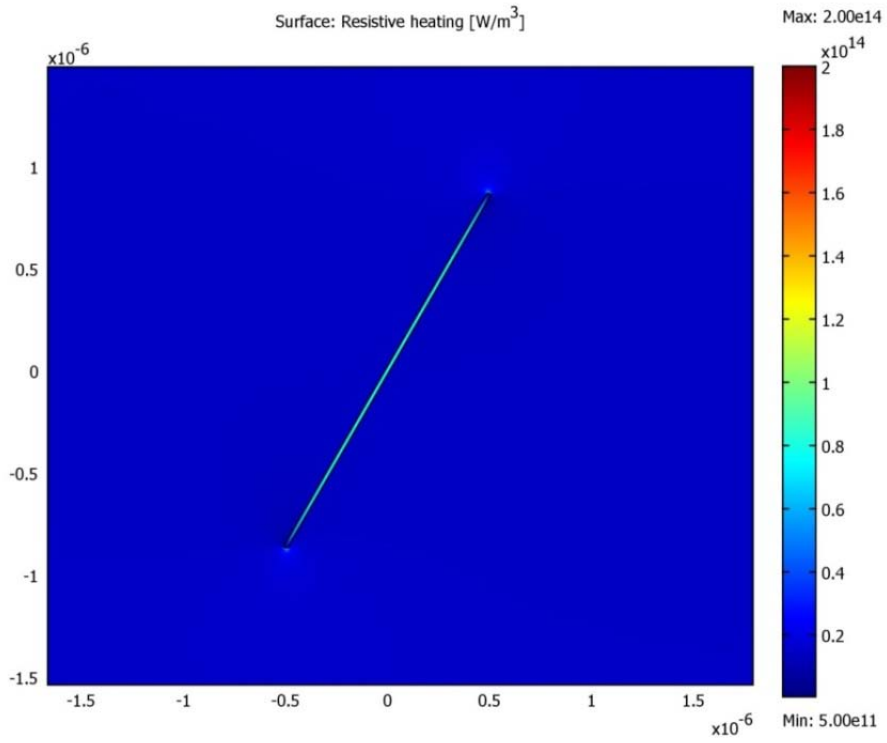
Very interestingly, the directions of cementite plate with respect to the current direction have very strong impact on the way that cementite fragments are heated compared to the matrix. This is wonderfully highlighted in Fig. 2.2 plots showing how cementite can become colder than matrix to hotter than matrix depending on its direction.



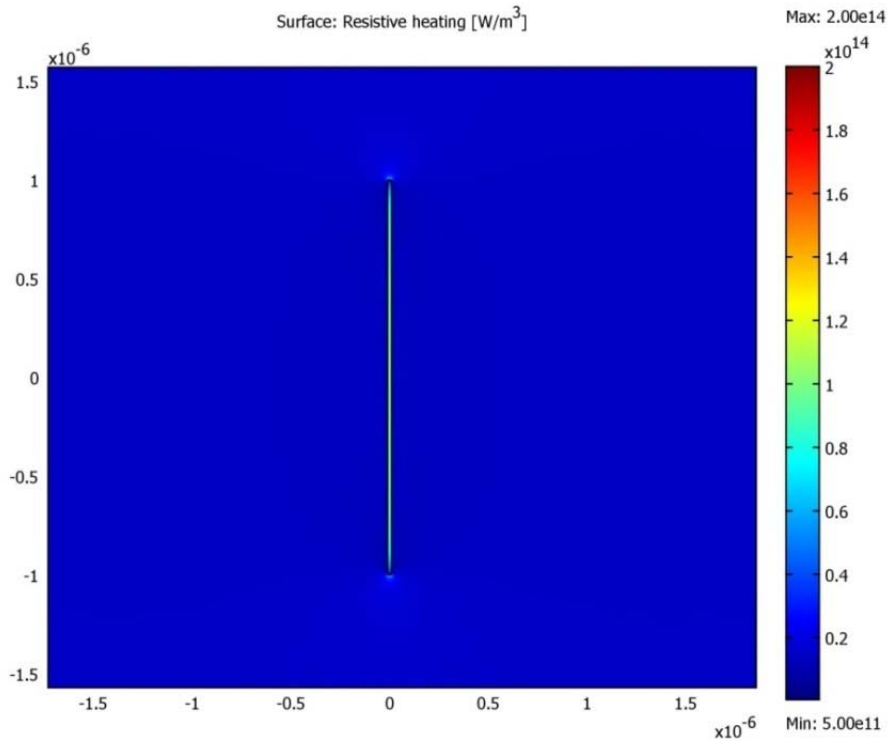
(a)



(b)



(c)



(d)

Fig 2.2: surface plot showing heating rate around a cementite plate for matrix current density of 10^{10} A/m² when it is aligned at (a) 0° (b) 30° (c) 60° (d) 90°

However for very short time of treatment , the total heat generated is so little that the heat effect on phase transformation can be neglected, leading the way for other physical phenomena to happen due to electricity.

2.8 Boundary condition for electromagnetic simulation

Input electric voltage is taken as 6000 Volt. The faces open to air is assumed to be fully insulating. At the phase boundary, electric potential is a continuous variable.

2.9 Relation to thermodynamics

From Maxwell Faraday equation we have,

$$\nabla \times \mathbf{E} = -\frac{\partial \mathbf{B}}{\partial t} \quad (2.24)$$

Maxwell Ampere law gives us

$$\nabla \times \mathbf{H} = \mathbf{J}_f + \frac{\partial \mathbf{D}}{\partial t} \quad (2.25)$$

And under steady state assumption (absence of time varying electric displacement field) it reduces to

$$\nabla \times \mathbf{H} = \mathbf{J} \quad (2.26)$$

Now consider a small volume element dV with charge density ρ and drift velocity \mathbf{v}_d causing a current density of \mathbf{j} in it. The work done by the electric field during a time δt is

$$dW = \delta t \int \mathbf{F}_e \cdot \mathbf{v}_d \quad (2.27)$$

$$\text{Or, } dW = \delta t \int \mathbf{E} \rho dV \cdot \mathbf{v}_d$$

$$\text{But } \mathbf{J} = \rho \mathbf{v}_d \quad (2.28)$$

$$\text{So, } dW = \delta t \int \mathbf{E} \cdot \mathbf{j} dV \quad (2.29)$$

Using (2.26)

$$dW = \delta t \int \mathbf{E} \cdot (\nabla \times \mathbf{H}) dV \quad (2.30)$$

From vector triple product rule

$$dW = \delta t \int \nabla \cdot (\mathbf{E} \times \mathbf{H}) dV - \delta t \int \mathbf{H} \cdot (\nabla \times \mathbf{E}) dV \quad (2.31)$$

Over an infinite surface, the first integral becomes zero. Using equation (2.24) in the 2nd part

$$dW = -\int \mathbf{H} \cdot \partial \mathbf{B} dV \quad (2.32)$$

Free energy change of the system should have opposite sign of work done to it,

$$dF = \int \mathbf{H} \cdot \partial \mathbf{B} dV \quad (2.33)$$

When the system is in steady state, this leads to,

$$dF = \frac{1}{2} \int \mathbf{H} \cdot \mathbf{B} dV \quad (2.34)$$

Magnetic vector potential \mathbf{A} is related to magnetic field as

$$\mathbf{B} = \nabla \times \mathbf{A} \quad (2.35)$$

So (2.34) reduces to

$$dF = \frac{1}{2} \int \mathbf{H} \cdot (\nabla \times \mathbf{A}) dV \quad (2.36)$$

$$\text{Or, } dF = \frac{1}{2} \int \mathbf{A} \cdot (\nabla \times \mathbf{H}) dV - \frac{1}{2} \int \nabla \cdot (\mathbf{H} \times \mathbf{A}) dV \quad (2.37)$$

The 2nd part of the integral being zero

$$dF = \frac{1}{2} \int \mathbf{A} \cdot (\nabla \times \mathbf{H}) dV$$

Using (2.26)

$$dF = \frac{1}{2} \int \mathbf{A} \cdot \mathbf{J} dV \quad (2.38)$$

So if we can express the magnetic vector potential in terms of electric current that is generating it, then we can get the change in free energy as a function of current flow in the system.

From (2.35)

$$\nabla \times \mathbf{B} = \nabla \times \nabla \times \mathbf{A} \quad (2.39)$$

$$\text{Or, } \nabla \times \mathbf{B} = \nabla(\nabla \cdot \mathbf{A}) - \nabla^2 \mathbf{A} \quad (2.40)$$

The first term in the right hand side being zero by Coulomb gauge condition

$$\nabla \times \mathbf{B} = -\nabla^2 \mathbf{A} \quad (2.41)$$

But from (2.26) and

$$\mathbf{B} = \mu \mathbf{H} \quad (2.42)$$

$$\nabla \times \mathbf{B} = \mu \mathbf{J} \quad (2.43)$$

$$\text{So, } \nabla^2 \mathbf{A} = -\mu \mathbf{J} \quad (2.44)$$

Which is basically a Poisson equation with a general solution of

$$\mathbf{A} = \frac{\mu}{4\pi} \int \frac{\mathbf{J}}{\mathbf{r}} dV \quad (2.45)$$

This result shows that to estimate magnetic vector potential at any point, we need to integrate the whole system. So current density in all the elements and their distance from this particular element under consideration will be significant.

Then the electromagnetic component of free energy for a particular element dV takes the form

$$\Delta F_{dV} = dV \frac{\mu}{4\pi} \int \frac{\mathbf{J} \cdot \mathbf{J}'}{|\mathbf{r} - \mathbf{r}'|} dV' \quad (2.46)$$

Here integration is done over the variables marked prime, to obtain the magnetic vector potential for the element dV . For electromagnetic free energy of the whole system, integration is done all over again for all such elements to finally get a form

$$F = \frac{\mu}{8\pi} \iint \frac{\mathbf{J} \cdot \mathbf{J}'}{|\mathbf{r} - \mathbf{r}'|} dV dV' \quad (2.47)$$

This equation will be extensively used for simulating thermodynamic effect of electropulsing.

To evaluate this integral numerically, discrete formulation is done as,

$$F = \frac{\mu}{8\pi} \Delta V^2 \sum_{i=1}^{i=n} \sum_{j=i}^{j=n} \frac{j_x j_x' + j_y j_y' + j_z j_z'}{\sqrt{(r_x - r_x')^2 + (r_y - r_y')^2 + (r_z - r_z')^2}} \quad (2.48)$$

Where ΔV is the volume of equal sized elements used for numerical integration and

$$\mathbf{J} = j_x \hat{\mathbf{i}} + j_y \hat{\mathbf{j}} + j_z \hat{\mathbf{k}}$$

$$\mathbf{J}' = j_x' \hat{\mathbf{i}} + j_y' \hat{\mathbf{j}} + j_z' \hat{\mathbf{k}}$$

$$\mathbf{R} = r_x \hat{\mathbf{i}} + r_y \hat{\mathbf{j}} + r_z \hat{\mathbf{k}}$$

$$\mathbf{R}' = r_x' \hat{\mathbf{i}} + r_y' \hat{\mathbf{j}} + r_z' \hat{\mathbf{k}}$$

As it is a double integration, if we do this for a 256^3 system, it will actually calculate 2^{48} (almost 3 quadrillion) steps and add them up, thus taking a very long time on a normal computer. So it is wiser to restrict to 2D simulation. As an example, 256×256 elements integration will need 2^{32} steps (a little more than 4

million) and thus will be finished in a much small time, still providing very indicative results. To do this 2D version of equation (2.48) is used.

$$F = \frac{\mu}{8\pi} \Delta a^2 \sum_{i=1}^{i=n} \sum_{j=i}^{j=n} \frac{j_x j_x' + j_y j_y'}{\sqrt{(r_x - r_x')^2 + (r_y - r_y')^2}} \quad (2.49)$$

Where Δa is the area of equal sized elements used for numerical integration and

$$\mathbf{J} = j_x \hat{\mathbf{i}} + j_y \hat{\mathbf{j}}$$

$$\mathbf{J}' = j_x' \hat{\mathbf{i}} + j_y' \hat{\mathbf{j}}$$

$$\mathbf{R} = r_x \hat{\mathbf{i}} + r_y \hat{\mathbf{j}}$$

$$\mathbf{R}' = r_x' \hat{\mathbf{i}} + r_y' \hat{\mathbf{j}}$$

2.10 Geometry for excess free energy calculation

As electromagnetic force is a long range, theoretically, we should do integration throughout the conductor to get precise electrical free energy. However as nanostructured object is being dealt with (ferrite cementite layered structure in pearlite), to understand and study the changes happening due to electropulsing down to nanometer level, we need to also simulated geometries of nanometer scale. This along with the computational complexity involved with 3 dimensional simulations, is the reason behind doing all trend analysis simulation in 2D.

For this a large ferrite matrix of 3 cm X 2 mm and single cementite structure or its broken components are placed.

To closely resemble gradual breaking down process the following geometrical configurations have been studied to observe the effects of microstructure on electromagnetic free energy.

- a) single cementite plate of $2\mu\text{m} \times 20 \text{ nm}$ dimension
- b) four broken parts of $0.5\mu\text{m} \times 20 \text{ nm}$ size
- c) eight parts of $250 \text{ nm} \times 20 \text{ nm}$ dimension
- d) sixteen broken parts of $125 \text{ nm} \times 20 \text{ nm}$ dimension

- e) thirty two parts of 62.5 nm x 20 nm size
- f) fifty equal parts of 40 nm x 20 nm size
- g) one hundred small cubes of 20 nm x 20 nm dimension
- h) a mixture of 200 nm x 20 nm, 80 nm x 20 nm, 60 nm x 20 nm, 40 nm x 20 nm, 20 nm x 20 nm sized cementite particles, five of each types

For exact thermodynamic energy evaluation in 3D, again in a large ferrite matrix of 3cm X 2mm X 2mm, a single cementite rod of 2 μm X 20 nm X 20nm or it's small 100 cube shaped broken parts are positioned in the center.

2.11 Results for energy calculations

Electromagnetic free energy monotonically decreases on breaking down the cementite plate even without any change in conductivities.

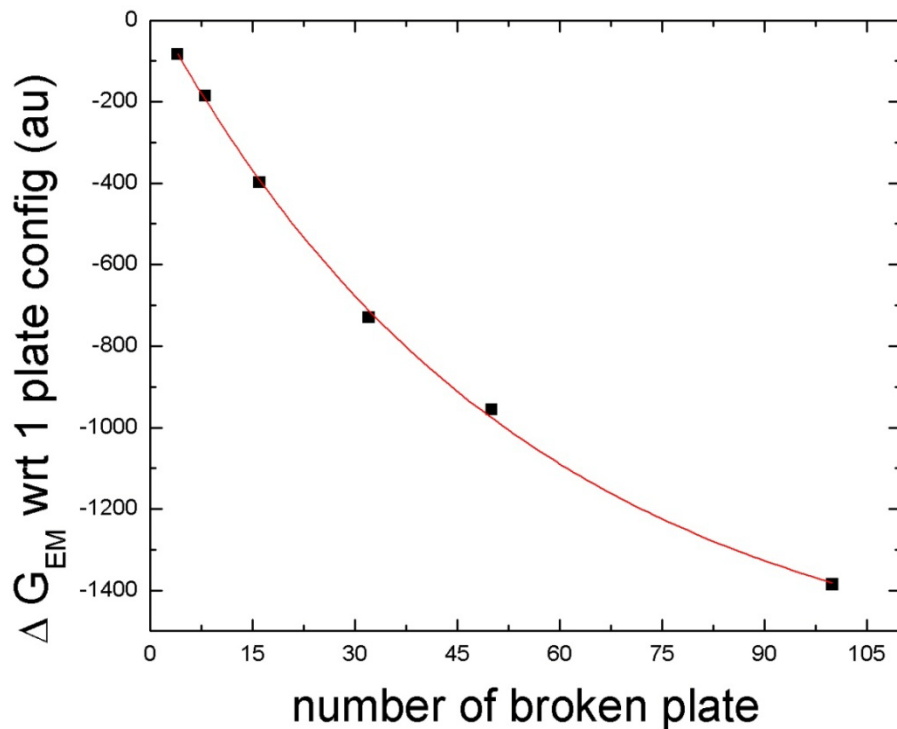


Fig 2.3: trend of change in electromagnetic free energy when a single plate of cementite (both relaxed and at room temperature) are broken into smaller parts

This result is very significant as it shows under electropulsing condition smaller cementite particles are more stable. In spheroidization reaction, the process is similar as the aspect ratio of cementite decreases over time to get a more particle like form [Chattopadhyay and Sellars, 1977, 1982]. But surface free energy plays vital role there. To make surface energy less than initial, the resulting particles have much higher diameter than the starting cementite plate thickness. But that is not the case here. All the structures calculated have same thickness. So very fine resulting cementite particle can be obtained is starting plates are thin enough.

Speaking of surface free energy, to know whether the electromagnetic energy lowering can overcome the increase in surface free energy to make the process thermodynamically possible, a few 3D simulations are done calculating the actual energy difference for complete breakdown to particles. The results as follows

Temperature (K)	Change in electromagnetic free energy for breakdown (mJ)
293	-2.96
473	-0.60

Clearly this is orders of magnitude larger than the increase in surface free energy (4×10^{-14} J). This high value obtained is due to the very high voltage (driving very high current of $\sim 5 \times 10^{11}$ Amp m^{-2}) used for simulation and due to the magnetic permeability of pearlite. At a current density of 10^7 A cm^{-2} and unit relative permeability ΔG_{EM} reduces to -2×10^{-14} J (due to the 2nd order relation of ΔG_{EM} with current density) and unable to overcome surface free energy increment. Under this electropulsing condition ΔG_{EM} obtained is similar in value to what other researchers have suggested for solidification under electropulsing condition [Qin *et al.*, 1998]. At a current density of 10^{10} Amp m^{-2} , and at room temperature, Change in electromagnetic free energy for breakdown in our system will be in the order of micro joules (experimental situation described later on).

To further investigate other factors' thermodynamic impact in success of structure

modification of pearlite by electropulsing simulations were done to know how resistivity of cementite ferrite and process temperature changes the lowering of electromagnetic free energy when single cementite breaks into large number of particles.

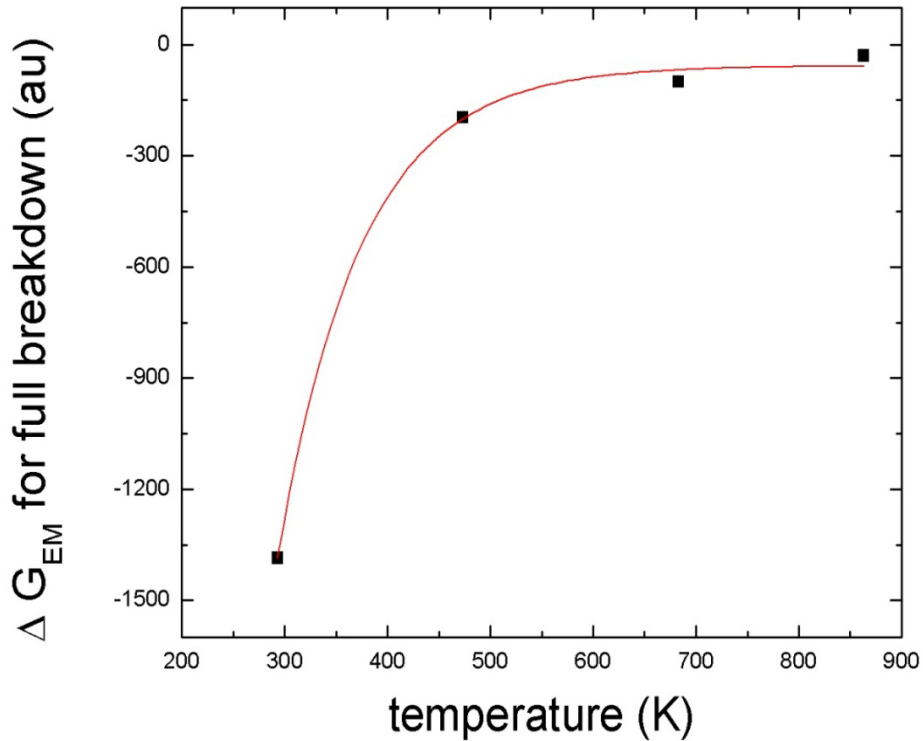


Fig. 2.4: Change in electromagnetic free energy due particle formation from single unbroken cementite at different temperatures

At different temperatures conductivities of ferrite and cementite are different. This results in different current distribution. Obviously the electromagnetic free energy change of breaking also gets affected. Significant point to be noted in this result that <200K increment in temperature can decrease $-\Delta G_{EM}$ drastically, rendering electropulsing ineffective. So our target should be to do the experiment as close to room temperature as possible by cancelling out joule heating.

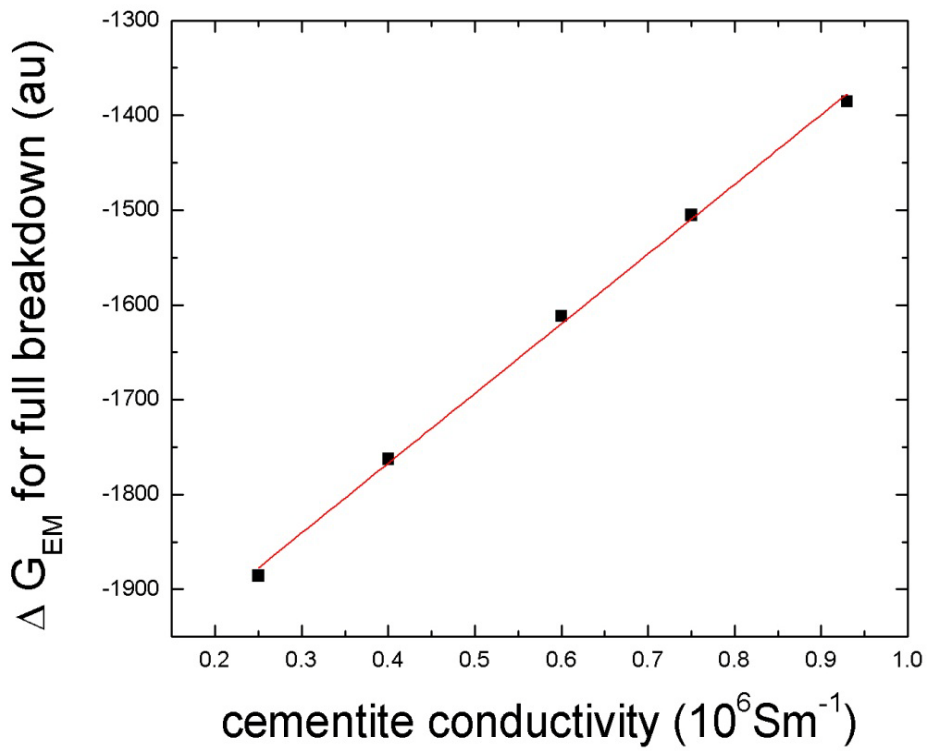


Fig. 2.5: Change in electromagnetic free energy due particle formation from single unbroken cementite at varying cementite conductivity

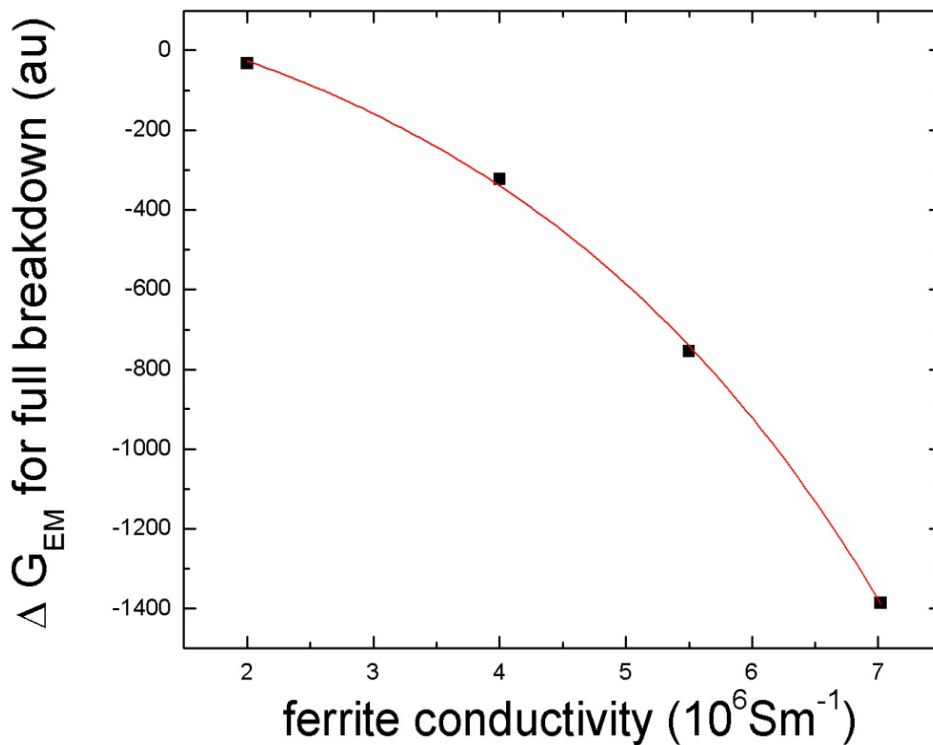


Fig. 2.6: Change in electromagnetic free energy due particle formation from single unbroken cementite at varying ferrite conductivity

Closely looking at Fig 2.5 and Fig. 2.6 it is understood that the fine microstructure formation process is thermodynamically more favorable when the matrix phase has very high conductivity and the embedded phase have very low conductivity. This is one crucial reason behind electropulsing based pearlite microstructure evolution having high chance of success.

2.12 Perspective on equivalent resistivity

Let us consider a uniform piece of conductor carrying current. Current density inside it will be uniform everywhere and equal to J_e . So the total electromagnetic free energy equation reduces to

$$F = \frac{\mu}{8\pi} \mathbf{J}_e \cdot \mathbf{J}_e \iint \frac{1}{|\mathbf{r} - \mathbf{r}'|} dV dV' = \frac{\mu}{8\pi} \mathbf{J}_e \cdot \mathbf{J}_e \mathbf{I}$$

$$\text{Where, } I = \iint \frac{1}{|\mathbf{r} - \mathbf{r}'|} dV dV'$$

The quantity I is dependent on the geometry of the object. So the total EM free energy will depend solely on the current density \mathbf{J}_e , which is again directly proportional to the conductivity of the material (σ). This shows that how large impact conductivity has on overall EM free energy because doubling the conductivity will account for four times the EM free energy.

Extending this concept to an object of unknown microstructure (black box model) we should always be able to find out an equivalent uniform current density which corresponds to same electromagnetic free energy due to the complicated current distribution across the micro structured material.

So modeling equivalent conductivity for any microstructure will give insight into how stable the structure will be under electropulsing condition.

Chapter 3:

Experimental procedure

3.1 Electropulsing experiment setup

The main target of this work being the study of solid state phase transformation under the influence of electropulsing, target capability of the ECP system is highest possible electric current density [Zhou *et al.*, 2002, 2002b, 2002c, 2003, 2004; Zhang *et al.*, 2002]. Drastic change in microstructure and atom arrangement is expected as per the simulation studies explained before, even on application of single pulse.

To achieve this electropulsing instrument is developed with the following components.

The main energy storage was done with a bank of 1200 μF 1800V capacitors. These are connected in series to achieve higher working voltage. The total voltage difference from end to end is apportioned to each capacitor. The entire series acts as a capacitor smaller than any of its components according to the inverse of its capacitance following this relation

$$\frac{1}{C_{eq}} = \frac{1}{C_1} + \frac{1}{C_2} + \dots + \frac{1}{C_n} \quad (3.1)$$

This is charged to a relatively high voltage (>4 kV) using a step up transformer and a rectifier.



Fig. 3.1: Capacitor bank and its charging setup

A xenon flash is used as trigger for the capacitor discharge circuit. The electrodes of the lamp are connected to the capacitor bank. The gas, however, exhibits extremely high resistance, and the lamp will not conduct electricity until the gas is ionized. Once ionized under very high potential difference, a spark forms between the electrodes, allowing the capacitor to discharge. The sudden surge of electric current quickly heats the gas to a plasma state, where electrical resistance becomes very low and the discharge process starts.

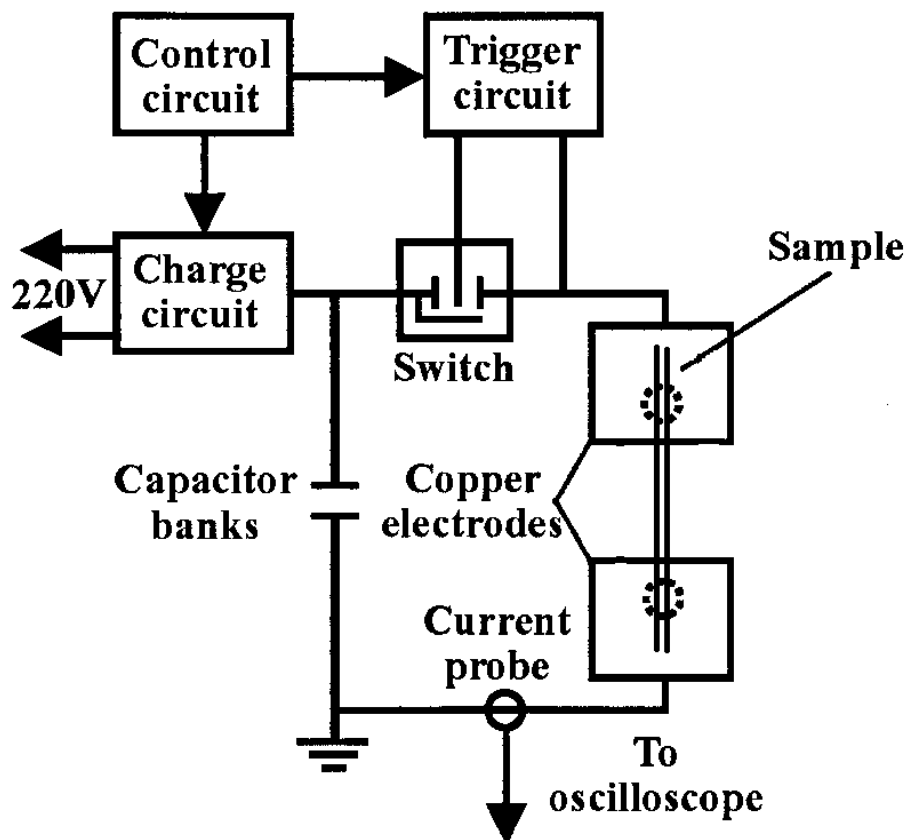


Fig. 3.2: Schematic representation of the electropulsing instrument

To promote room temperature changes, all electropulsing experiments have to be done in ambient situation and to avoid heating effect as much as possible, the electrodes used are made of copper and large in size. This ensures that the sample dissipates any heat generated extremely fast. The pulsed length of the wire shaped sample is 30 mm which lies between the two large electrodes as seen in the image taken.



Fig. 3.3: The large copper electrode cum heat sink used for electropulsing the steel samples

The waveform of the pulsed discharge system is basically a damped oscillation. To detect the electric pulse in a non-contact manner, a Rogowski coil based system was used. A Rogowski coil is an electrical device for measuring alternating current (AC) or high speed current pulses. It consists of a helical coil of wire with the lead from one end returning through the center of the coil to the other end, so that both terminals are at the same end of the coil. The whole assembly is then wrapped around the straight conductor whose current is to be measured. Since the voltage that is induced in the coil is proportional to the rate of change of current in the straight conductor, the output of the Rogowski coil is usually connected to an integrator circuit in order to provide an output signal that is proportional to current pulse.

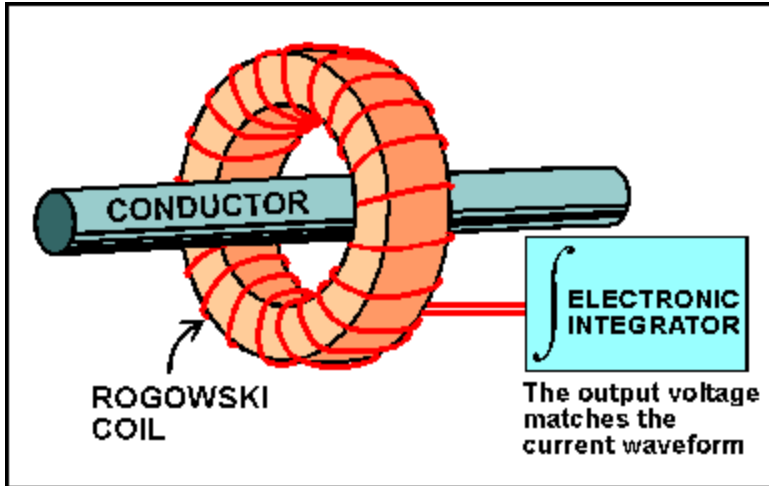


Fig. 3.4: Rogowski coil - in absence of any iron core to saturate magnetically, the output is inherently linear.

The output of this is studied using a Tektronix TDS3012 digital storage oscilloscope. As seen in the oscilloscope the whole pulse died down in around 800 μsec and had an oscillation time of 120 μsec .

To convert the oscilloscope reading to the actual electropulsing current this relation has to be used for n loop coil

$$V_{osc} = \frac{1}{RC} \frac{nA\mu_0}{2\pi r} I_{ECP} \quad (3.2)$$

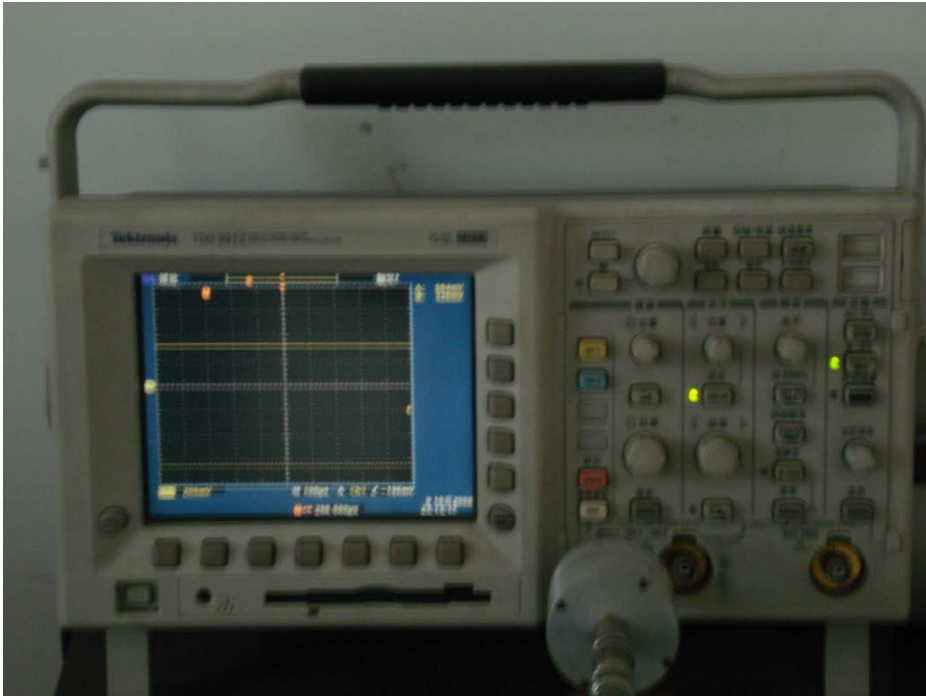


Fig. 3.4: Tektronix TDS 3012 digital storage oscilloscope: used for recording electric pulse.

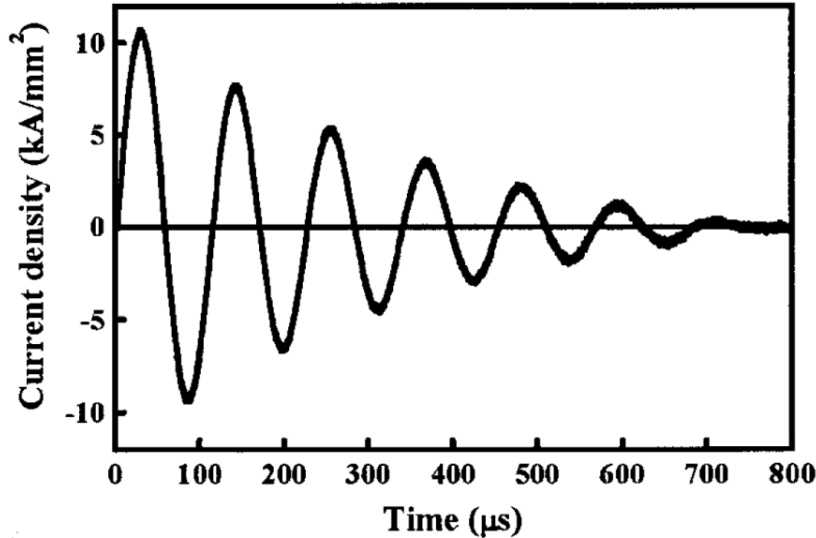


Fig. 3.5: Typical electropulsing waveform



Fig. 3.6: Electropulsing waveform as observed in the oscilloscope

3.2 X-ray Diffraction

Scientists and engineers extensively use powder X-ray diffraction techniques for rapid, non-destructive analysis of materials and structural studies. In a polycrystalline aggregate like our material is, if it is assumed that every possible crystalline sample is present in equal proportions we can neglect the particular positioning of the sample due to resulting orientation averaging. When the diffracted beam is collected on a flat plate detector the rotational averaging leads to smooth diffraction rings around the beam axis rather than the discrete Laue spots as observed for single crystal diffraction. The angle between the beam axis and the ring is called the scattering angle and in X-ray crystallography always denoted as 2θ . Powder diffraction data are usually presented as a diffractogram in which the diffracted intensity I is shown as function either of the scattering angle 2θ . As the diffractogram obeys Bragg's law, every crystalline material depending upon its

unique crystal structure and lattice spacing, have its distinctive diffraction pattern. Cylindrical electropulsed samples are grinded to half thickness to obtain a flat surface and then polished using silicone carbide paper. Diffraction experiments are done in a BRUKER D8 ADVANCE diffractometer. A scan step of 0.02° is used for all scans. Due to small specimen dimension, thin slit of 1 mm X 0.1 mm is preferred. Wavelengths associated with the copper target for X-ray generation are $K\alpha_1 = 1.540596 \text{ \AA}$ and $K\alpha_2 = 1.544493 \text{ \AA}$.

The intensity ratio of these two wavelengths is 2:1. This information is used for stripping off the $K\alpha_2$ component from experimental data before any analysis is done. For measurement of instrumental broadening, an alumina reference is used.

3.3 Optical microscopy

This is the most basic visible light based tool used in metallography. Nowadays CCD camera is used along with it for image capture and storage in computer format. Resolving power of an optical microscope is not very high due to longer wavelength of the light spectrum in visible range. Theoretical limit to resolving power is given by

$$d = \frac{\lambda}{2A_n}$$

For practical purpose a resolution of around $1\mu\text{m}$ can be assumed. Due to this limitation we can not use optical method for metallography as our drawn steel wires and electropulsed samples are expected to have very fine nanometer scale structure. However this can be used to have large scale overview.

Before putting into microscope, small samples are mounted into a composite powder for giving requisite size for holder and then polished and etched 3 % Nital or a solution of 1 g sodium meta-bisulfite in 100 ml water mixed with 4 g of picric acid dissolved in 100ml of water, for 30 sec. Olympus DMC2 microscope is used for taking optical micrographs.

3.4 Scanning electron microscopy

The scanning electron microscope (SEM) is a type of electron microscope that images the sample surface by scanning it with a high-energy beam of electrons in a raster scan pattern.

In a typical SEM, an electron beam is thermionically emitted from an electron gun fitted with a tungsten filament cathode. Tungsten is normally used in thermionic electron guns because it has the highest melting point and lowest vapor pressure of all metals, thereby allowing it to be heated for electron emission. However in the field emission kind of SEM used here emitter is of the Schottky type, in which thermionic emission is enhanced by barrier lowering in the presence of a high electric field. Schottky emitters are made by coating a tungsten tip with a layer of zirconium oxide, which has the unusual property of increasing in electrical conductivity at high temperature. FE-SEM electron beam is smaller in diameter, more coherent and with up to three orders of magnitude greater current density or brightness than can be achieved with conventional thermionic emitters. The electron beam, which typically has an energy ranging from a few hundred eV to 40 keV, is focused by one or two condenser lenses to a spot about 0.4 nm to 5 nm in diameter. The beam passes through pairs of scanning coils or pairs of deflector plates in the electron column, typically in the final lens, which deflect the beam in the x and y axes so that it scans in a raster fashion over a rectangular area of the sample surface. The electrons interact with the atoms that make up the sample producing signals that contain information about the sample's surface. Major benefit over optical microscopy include much better resolving power even up to 2 nm (250 times better than a optical microscope) and due to the very narrow electron beam, SEM micrographs have a large depth of field yielding a characteristic three-dimensional appearance useful for understanding the surface structure of a sample.

To actually get this 3D structure in surface, samples are etched with 3% Nital solution for about 20 seconds after mounting (due to the very small size of samples) grinding and polishing with silicon carbide papers. For giving ground contact to

non-conducting mounting composite, silver paste is used.

Finally electron microscopy is done with Zeiss Ultra-55 SEM machine.

3.5 Resistivity measurement

We are accustomed to writing the resistance of a conductor as $R = \rho_r(l/a)$. However the assumption that the current density is uniform throughout the conductor is not always valid. Suppose the conductor is not homogeneous, and this expression no longer holds. When current enters a conductor through a point contact, the current density in the sample immediately under the contact is very large. Then the current quickly spreads and becomes fairly uniform. At the exit contact, the current again must flow into the point contact. The effective sample resistance (even if it did not include lead and contact interface resistances) is not simply $\rho_r(l/a)$, due to the non-uniform current density. Even if the weight is evaluated by integration, it is critically sensitive to the exact contact area, which is hard to determine. A popular method known as four probe method is used to solve this problem in one dimensional geometry. Voltage drop is measured at the uniform current density region and basic laws can be used to estimate resistivity. This way issue of contact resistance is also dismissed. During experimentation, a constant current of 10 mA and 100 mA is driven through the sample by using a Keithley 224 constant current source and the voltage difference at two inner points by using Keithley 184 nano volt meter. All contacts are made with silver paste.

3.6 Hardness test

Hardness is not a true property of a material; however it is used by engineering widely for having idea about the yield strength of the material. Among many hardness measuring techniques and scales Vickers's hardness is popular for metals mainly due to its standardization and wide range covered. The unit of hardness in this scale is Vickers pyramid number (HV). Hardness in Vickers scale is

independent of the test force used from 500 gf to 50 kgf. To measure hardness in the pearlite sample, a WOOLPERT SVD 425 machine is used with 10 kgf force with a dwell time of 10 sec.

Chapter 4:

Experimental result and analysis

4.1 Choice of material

High carbon (0.8 wt%) steel is chosen in the present work because of two reasons: a). There is no any work on the effect of electropulsing on high carbon steels reported or published. The mechanism of electropulsing-induced microstructure transformation in metallic materials is not fully understood. Supplement of information on behavior of high carbon steels under electropulsing helps to improve the scientific understanding of metal-electropulsing interactions. b). There is a need to improve the mechanical property of high carbon eutectoid steel. Electropulsing is a potential way.

The as-cast samples are provided by POSCO. The microstructure is fully pearlitic, free from any pre-eutectoid precipitations. As mentioned before, our target was to study the effect of electropulsing on solid state transformation and to achieve drastic changes with just a single pulse. Therefore, we purposely push the system into a state which is far from equilibrium. This will increase the chance to observe the microstructure transformation during the evolution of materials from a non-equilibrium state to a near-equilibrium or even equilibrium thermodynamic states defined by electropulsing thermodynamics along with the other general parameters. To this, the as casted steel underwent severe cold rolling to a true strain of 3.00. This equals to 95% reduction in area and the final wire sample with diameter 1.23 mm.

It is suggested by others [Languillaume *et al.* 1997; Hong *et al.*, 1999; Nam *et al.*, 2000; Sauvage *et al.*, 2000; Hono *et al.*, 2001] that the pearlitic steels after severe deformation have high level of residual strain and dislocation density. And large amount of carbon in cementite can dissolve into ferrite, which possesses higher lattice parameter and is thermodynamically unstable. It has been noted from these works that cementite changes its primary crystal structure towards a more irregular

configuration.

4.2 Electropulsing

After consideration of parameter availability of electropulsing equipment and the requirement of theoretical predictions for electropulsing-induced phase transformation, three sets of discharge voltage levels were chosen and applied to the samples. The details are listed in table 4.1

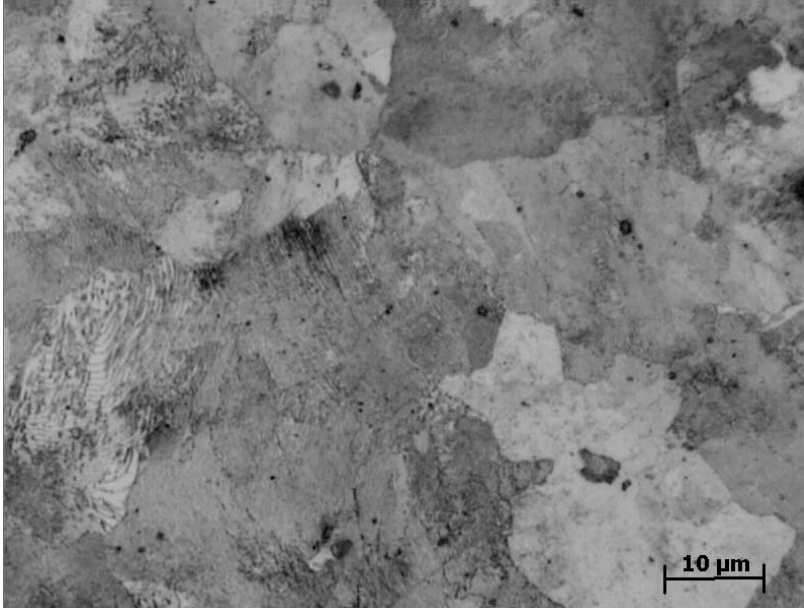
Table 4.1: Electropulsing parameters used

Sample name	Discharge voltage	Current density
EP19	4.8 kV	$7.73 \times 10^9 \text{ Amp/m}^2$
EP20	6.0 kV	$9.82 \times 10^9 \text{ Amp/m}^2$
EP21	6.6 kV	$1.07 \times 10^9 \text{ Amp/m}^2$

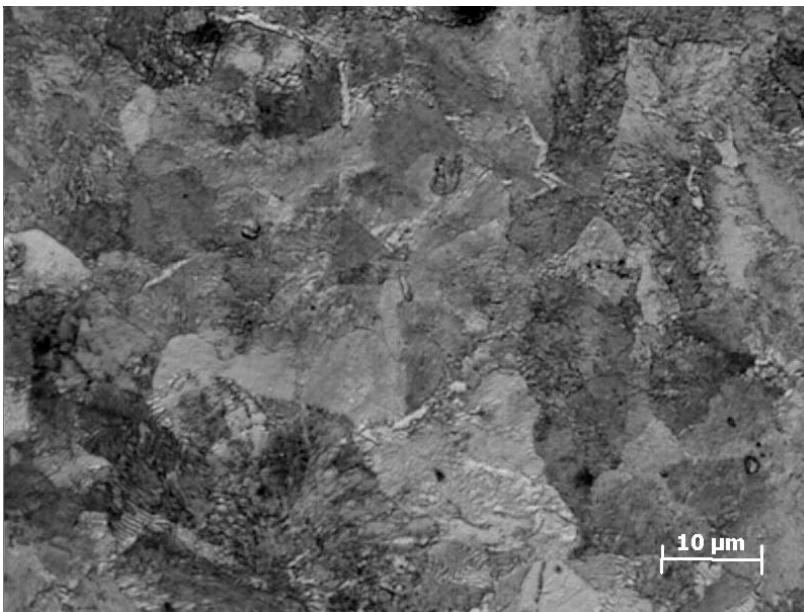
The samples are fixed between the copper clamps of electropulsing equipment. The distance between two clamps is around 30 mm. The electropulsed samples are taken apart afterwards for further investigation.

4.3 Optical microscopy

Optical microscopy is used to characterize the microstructure difference between the as cast alloy and cold drawn sample. According to expectation, microstructure changes from un-deformed grains (Fig. 4.1) to very fine pearlite colonies aligned in the rolling direction (Fig. 4.2).

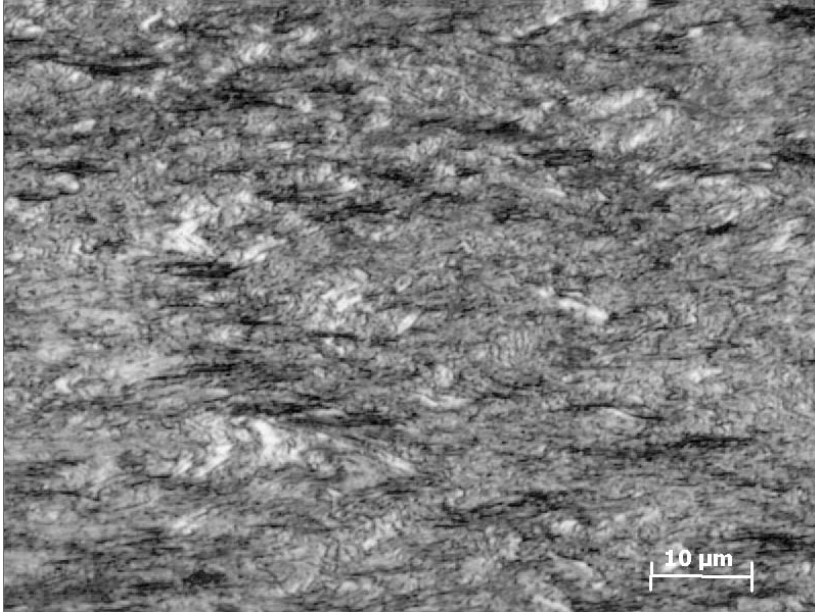


(a)

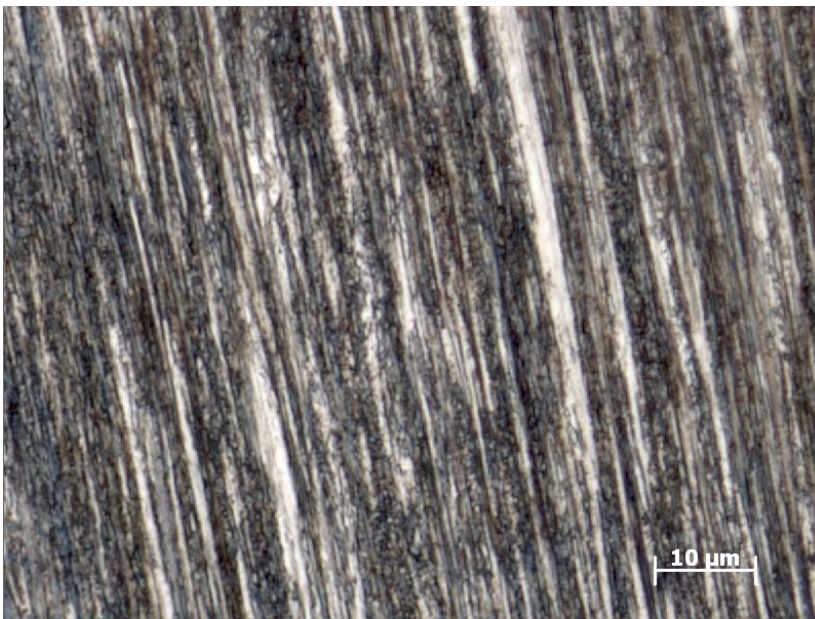


(b)

Fig. 4.1 Optical micrograph of as cast steel shows no-elongation (a) cross section and (b) longitudinal section.



(a)

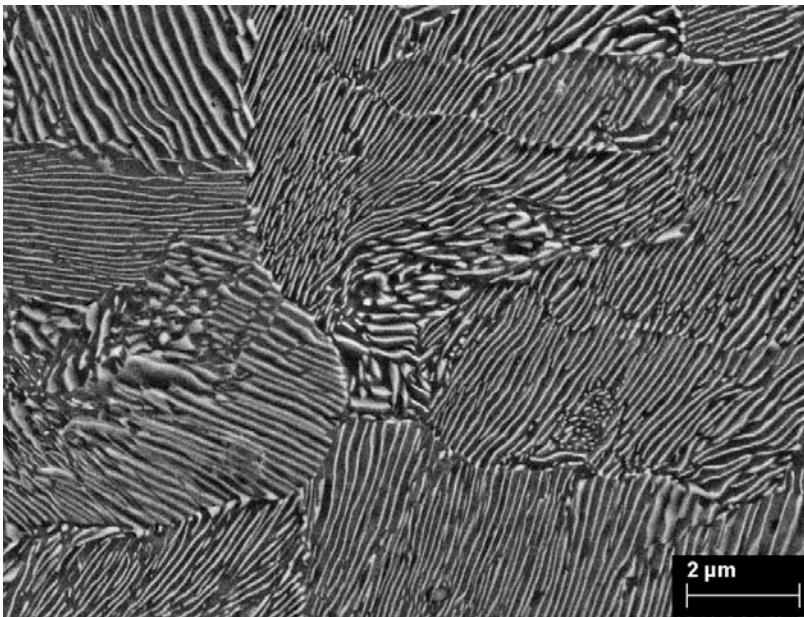


(b)

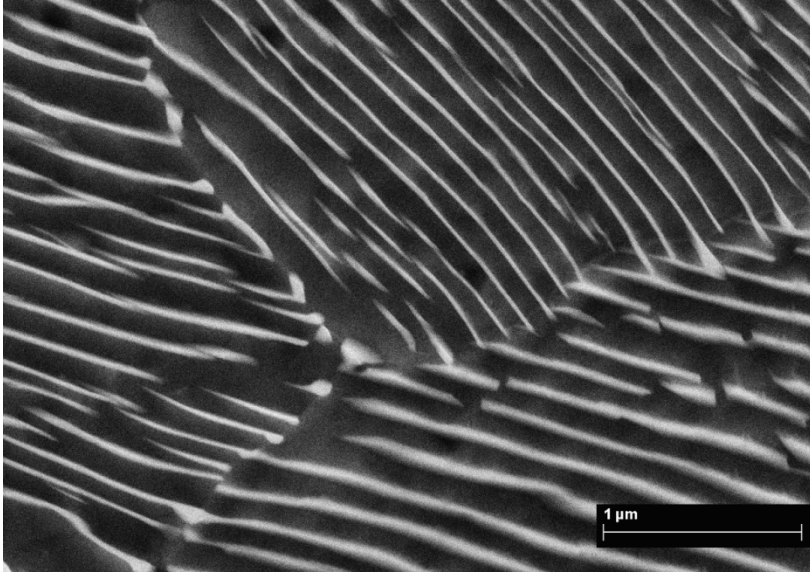
Fig. 4.2 OM of cold drawn steel sample shows elongated grains along the drawing direction (a) cross section and (b) longitudinal section.

4.4 Scanning electron microscopy

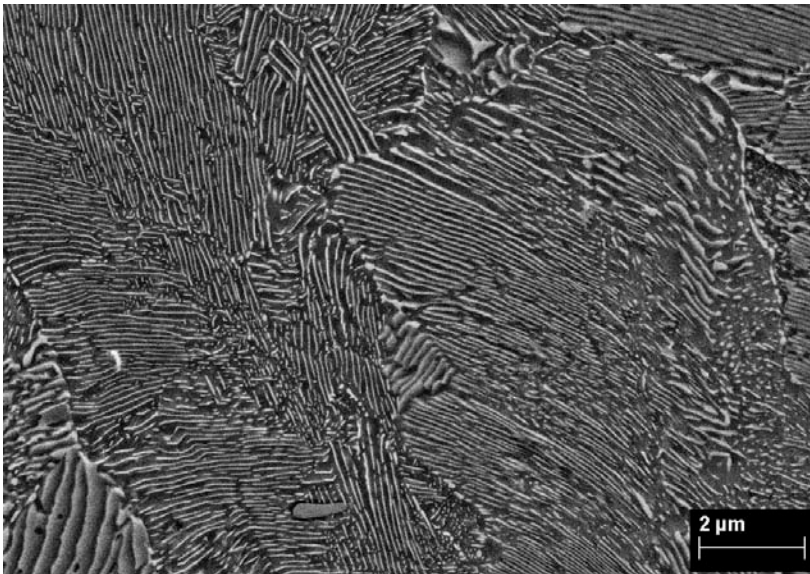
FE-SEM provides microstructural images with higher resolution than optical micrograph. Figure 4.3 demonstrates pearlite microstructures of un-deformed samples at both cross section and longitudinal sections at various magnifications. It can be seen that the microstructures are similar and orientations are random in both longitudinal and cross sections in as cast steel.



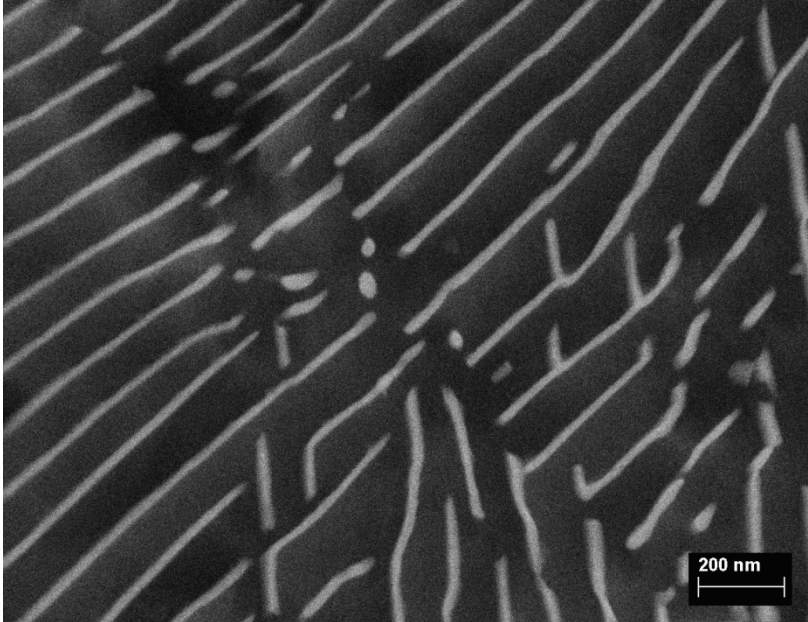
(a)



(b)



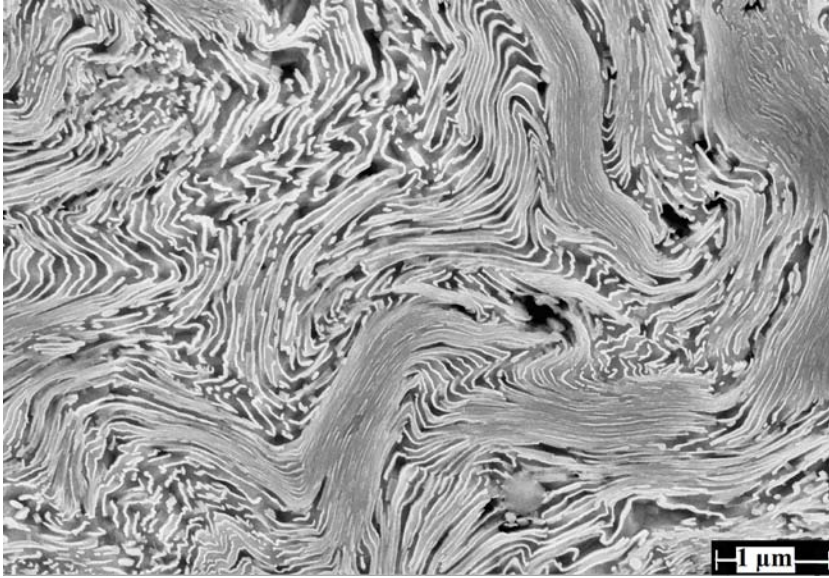
(c)



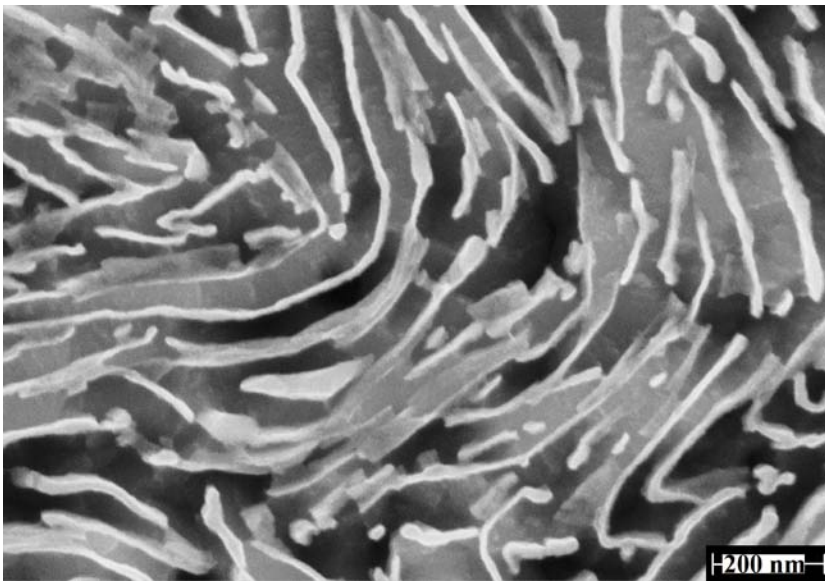
(d)

Fig. 4.3 SEM micrographs of as cast alloy shows randomly oriented fully pearlite grains. (a) and (b) cross sections. (c) and (d) longitudinal sections.

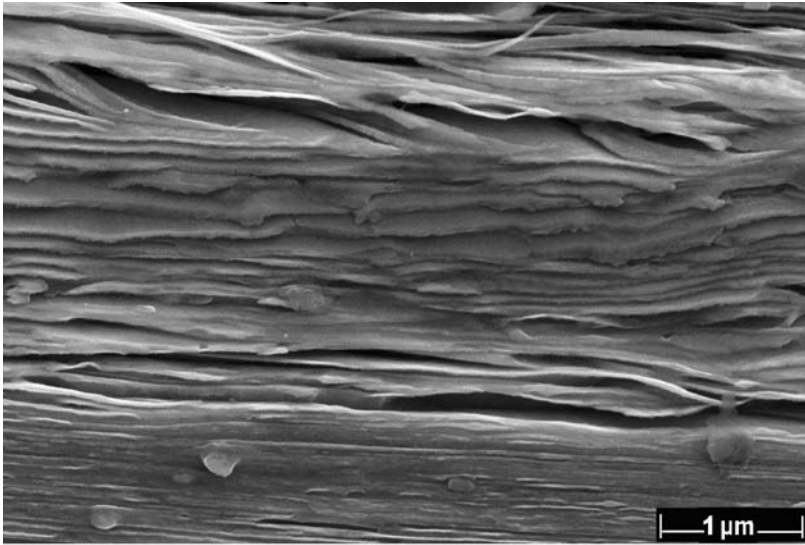
Severe deformation of pearlite steel causes drastic change in microstructure. In cross section view, pearlite colonies are crammed together [Zelin, 2002] and form wavy tangled pattern (fig 4.3 a-b). The inter-lamellar space decreases. These can be seen more obviously in the longitudinal section, as illustrated in figure 4.3 c-d. Very important observation in electroscopic observation is that no obvious grain boundary is identified in heavily cold drawn sample.



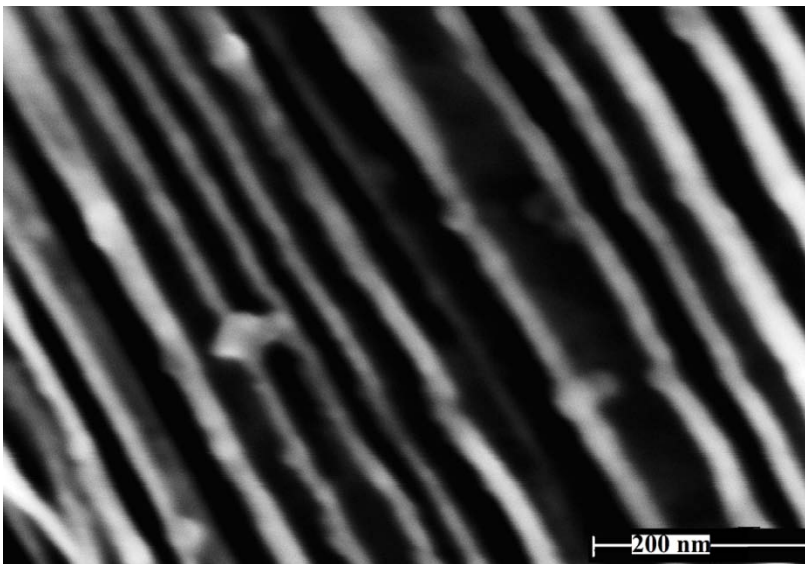
(a)



(b)



(c)



(d)

Fig. 4.4 SEM micrographs of deformed alloy show drastic change of microstructures. (a) and (b) cross sections. (c) and (d) longitudinal sections.

For electropulsed samples, SEM micrograph did not reveal any observable change in sample EP19, as is demonstrated in figure 4.5. However, very striking microstructures are observed in sample EP20 and EP 21. Very fine spheroidised

cementite particles replace the original elongated cementite lamellae. Figure 4.6 (a) and (b) are by EP20 sample in longitudinal section. Figure 4.5 (c) and (d) are by EP21 in the cross section.

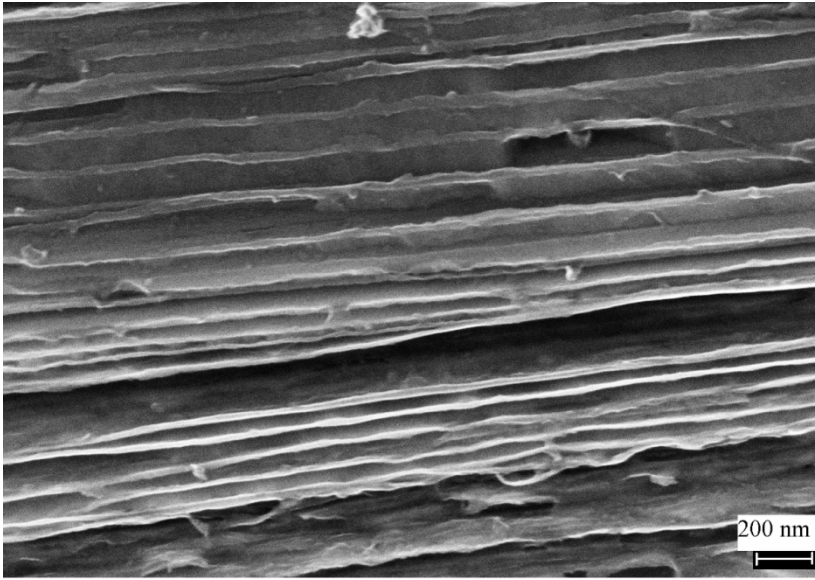
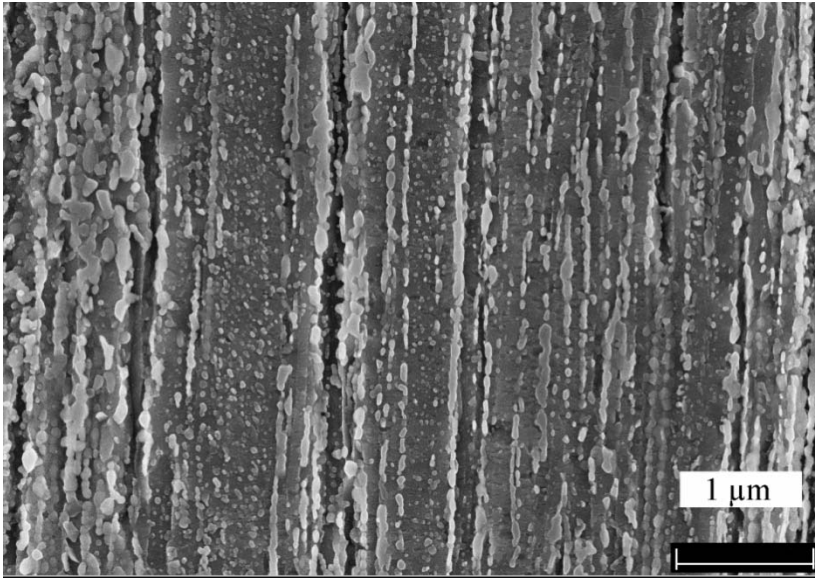
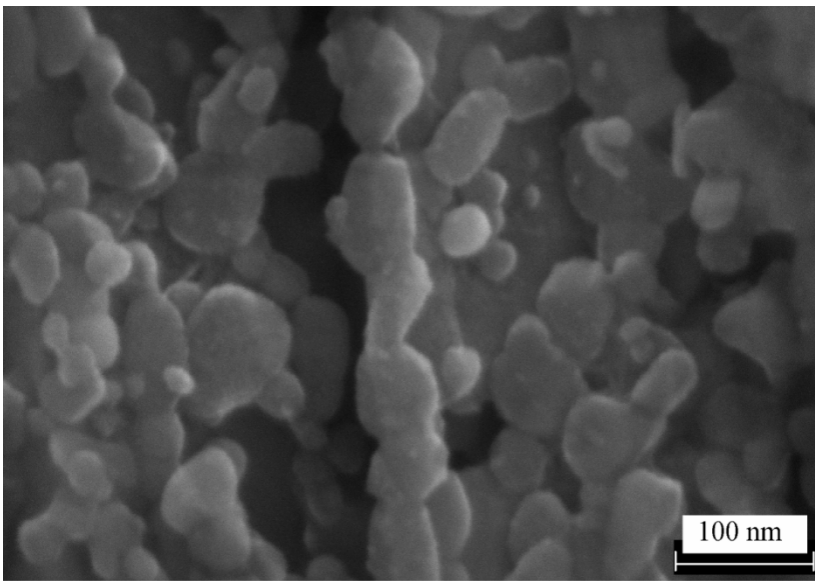


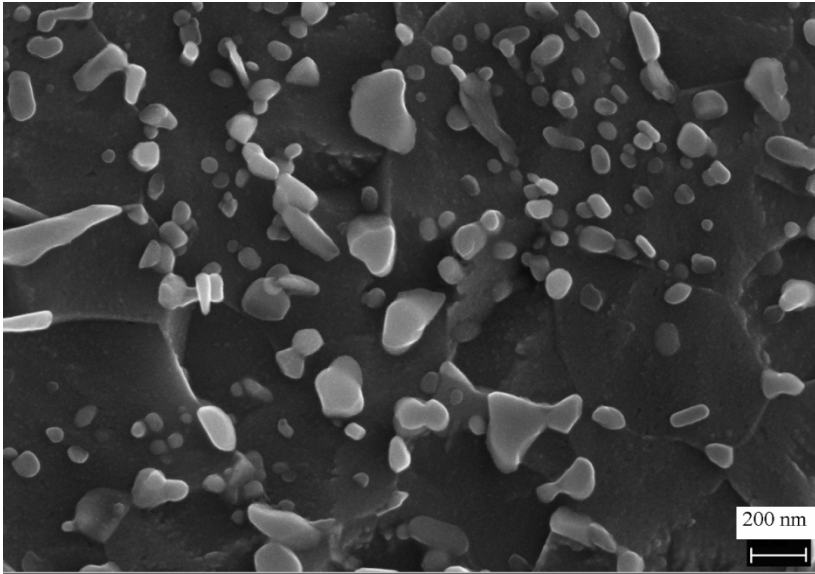
Fig. 4.5: SEM image of longitudinal section of EP19



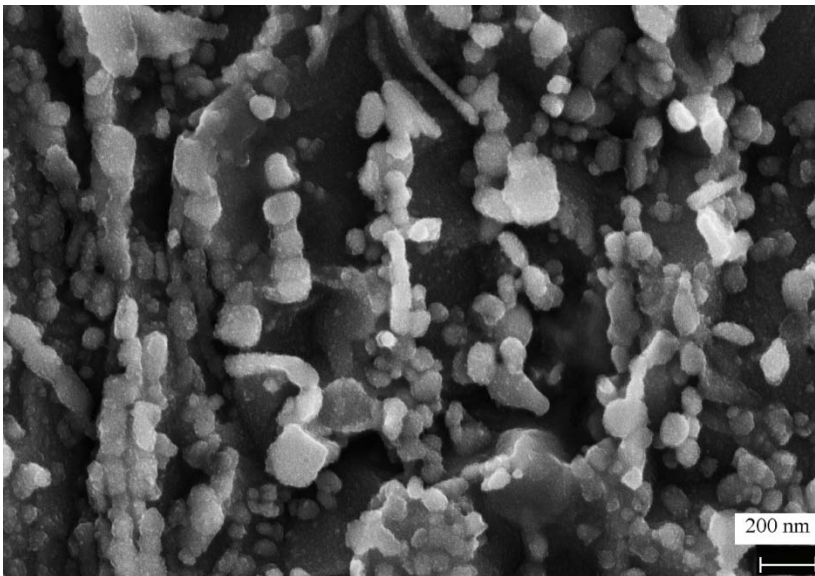
(a)



(b)



(c)



(d)

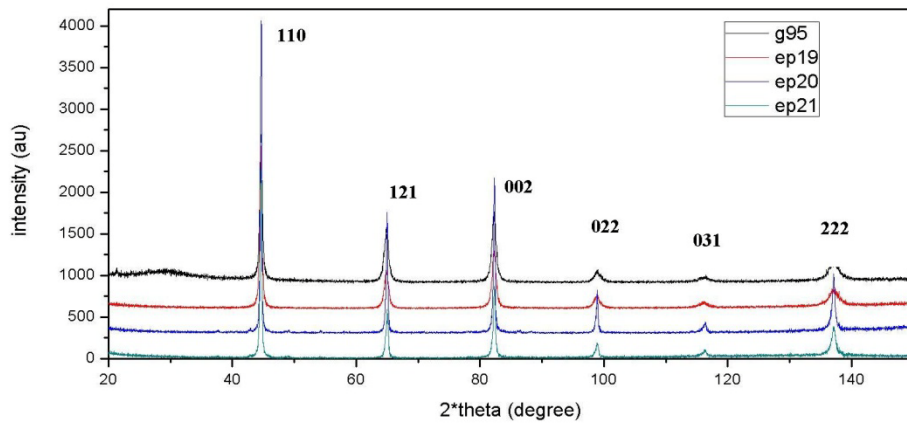
Fig. 4.6: Cementite particles formed by electropulsing treatment. (a) and (b) EP20 in longitudinal section; (c) EP21 in cross section and (d) EP21 in longitudinal section.

One important difference between microstructures in EP20 and EP21 samples is

that the cementite particles are more randomly distributed in EP21 than in EP20 samples. In EP20 sample, the original cementite lamella can be traced back, as can be seen in Figure 4.5 (a). It is less obviously in EP21 samples.

4.5 X-ray diffraction

The diffractograph for four samples are as follows. Clearly it shows less peak broadening in electropulsed samples. Ferrite peaks are marked.



X-ray diffraction (XRD) detects the change of lattice parameters. Four of those many reasons that cause change of XRD patterns are residual stress, grain size, local composition and texture. We identify microstructure change by analysis three kinds of changes in diffraction spectrum – position and width of resonance peaks. The interpretation of the change of those characteristic parameters to microstructure evolution will be discussed in following sections.

Diffraction peaks are fitted into a Lorentzian function (fig 4.6) and area under it (deducting y-shift) is taken as the peak intensity.

$$y = y_0 + \frac{2Ar}{\pi} \frac{w}{4(x - x_0)^2 + w^2} \quad (4.2)$$

Parameter w is full width at half maxima, x_0 is peak central, y_0 offset, Ar is area under curve.

To do this separate high quality scans are done for every peaks.

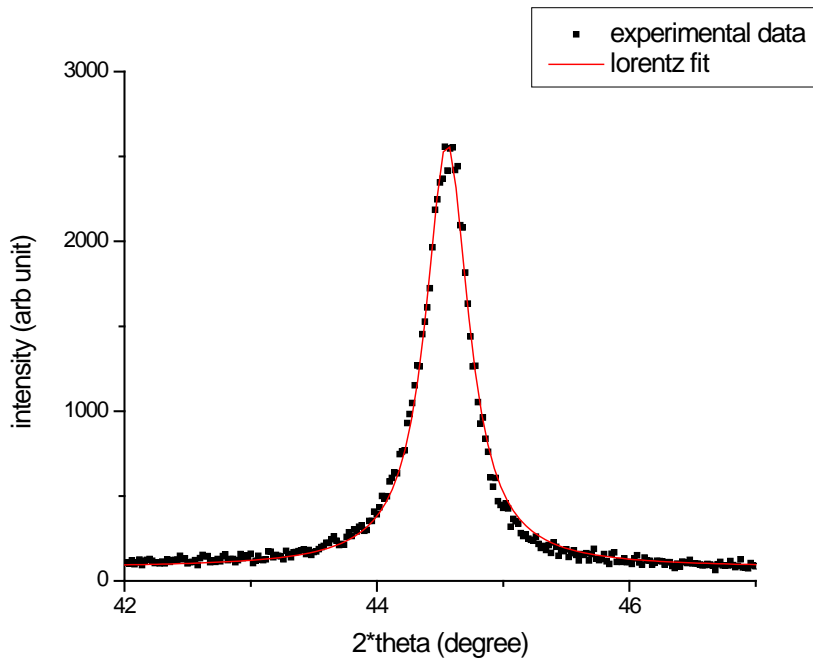


Fig. 4.6: Lorentz fitting of experimental data for 110 ferrite peak in sample EP19 sample

4.5.1 Alterations in peak positioning

Using Bragg's law peak position can be related to d-spacing as

$$\theta = \sin^{-1}\left(\frac{\lambda}{2d}\right) \quad (4.3)$$

D-spacing again can be calculated from miller index of the plane and cell parameter by following equations

$$\frac{1}{d^2} = \frac{h^2 + k^2 + l^2}{a^2} \quad (4.4)$$

where h, k, l are miller indices and a is cell parameter of a unit cubic cell (e.g., ferrite)

$$\text{Or, } \frac{1}{d^2} = \frac{h^2}{a^2} + \frac{k^2}{b^2} + \frac{l^2}{c^2} \quad (4.6)$$

where h, k, l are miller indices and a, b, c are cell parameter of a unit orthorhombic cell (e.g., cementite).

In a polycrystalline system like the steels considered in the present work the presence of solute atom can be easily detected and measured by precise parameter measurement which will be discussed later.

However there is a caveat in this seemingly easy procedure of determining lattice parameter. We need to keep in mind that Bragg's law contains $\sin \theta$ component. So the precision in d-spacing depends on the accuracy of $\sin \theta$. However at a higher angle, rate of change of $\sin \theta$ with respect to θ is very slow than at lower angle. More accurate measurement is, therefore, required at this stage (fig 4.7).

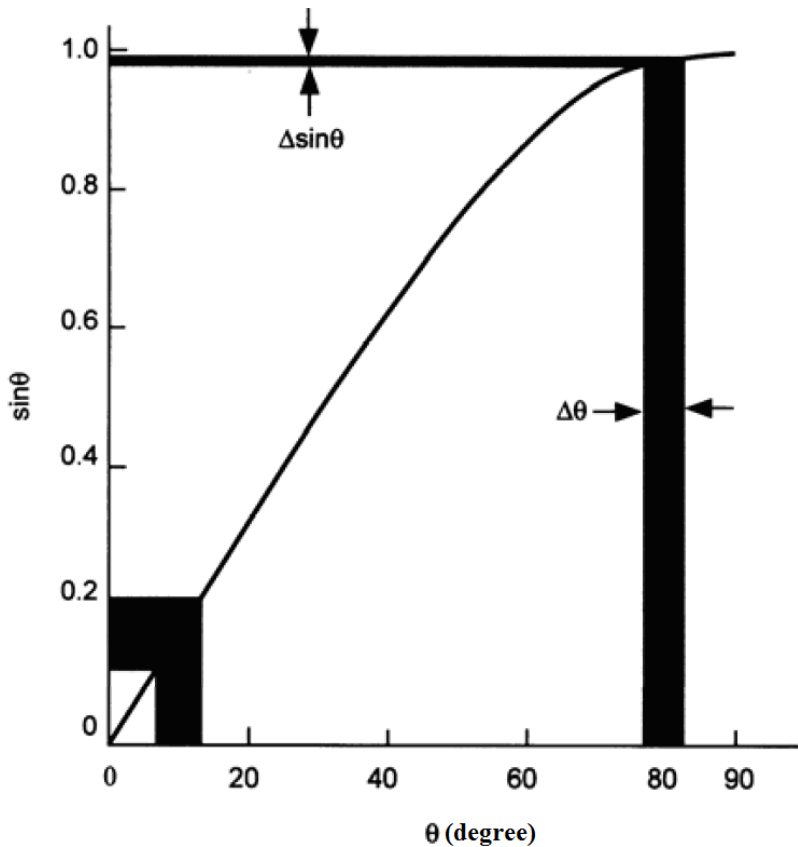


Fig. 4.7: The variation of $\sin \theta$ with θ . The error in $\sin \theta$ caused by a given error in θ decreases as θ increases

To have a numerical taste of this, Bragg's law is differentiated with respect to θ to get,

$$\frac{\Delta d}{d} = \frac{\Delta \lambda}{\lambda} - \cot \theta \Delta \theta \quad (4.7a)$$

As wavelength of X-ray is known precisely in experiments,

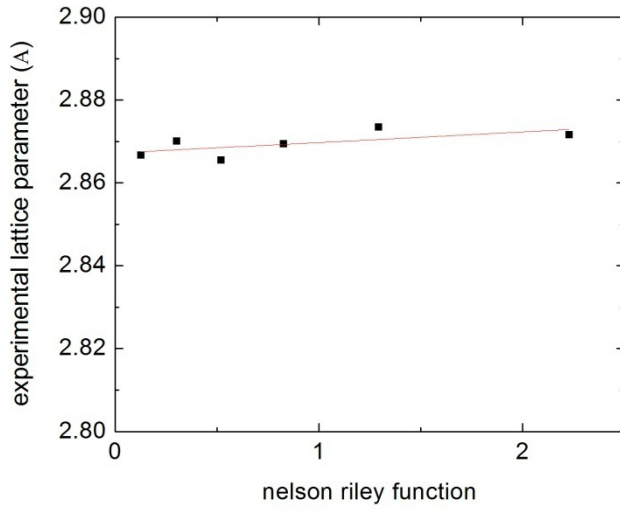
$$\frac{\Delta d}{d} = -\cot \theta \Delta \theta \quad (4.7b)$$

We need to keep in mind that ferrite do not have any peak in the vicinity of $\theta = 90^\circ$, which means that we cannot get a low error result without resorting to extrapolation. However the relation between error level and θ is non-linear. General extrapolation of this curve is not accurate. So we need to plot the measured value or lattice parameter against some function of θ so that the resulting curve becomes linear. This way we can get an accurate extrapolation. This function depends upon the geometry and the type of the instrument used. For Hall Debye Scherer type of camera, which is our case, a Nelson Riley extrapolation function is appropriate [Cullity, 2001] as error in determination of lattice parameter is a highly linear

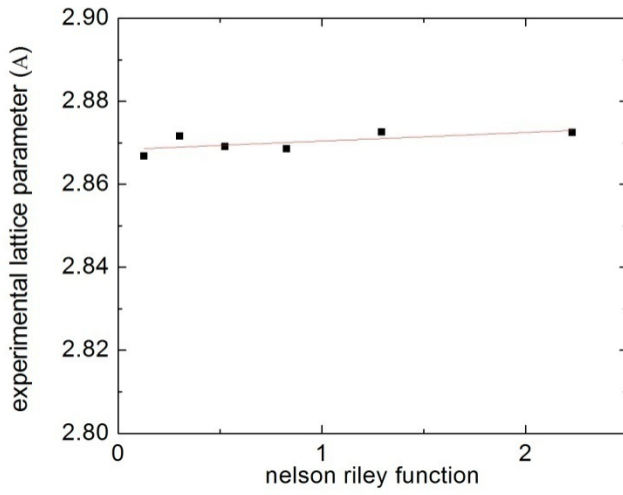
function of $\frac{\cos^2 \theta}{\sin \theta} + \frac{\cos^2 \theta}{\theta}$ even up to a very low value of θ . So Nelson Riley

function $\frac{1}{2} \left[\frac{\cos^2 \theta}{\sin \theta} + \frac{\cos^2 \theta}{\theta} \right]$ when plotted against measured lattice parameter

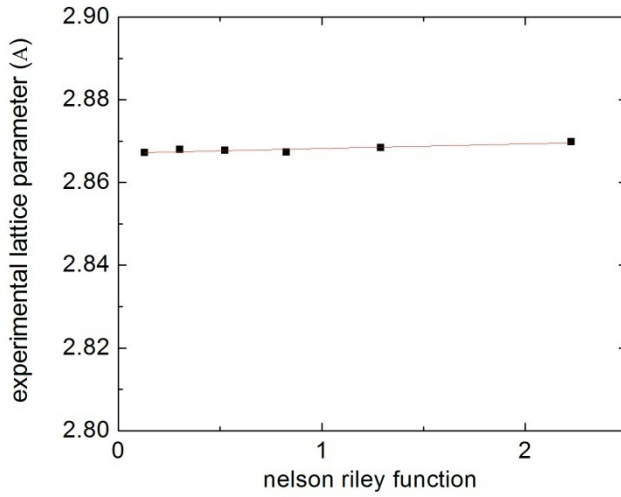
from each diffraction peaks, and extrapolation to $\theta = 90^\circ$, gives a very high precision lattice constant which in our case precise up to five significant digits following that precision in experimental measurement. This method gives precise enough result needed for determination of solute concentration [Lee and Lee, 2005].



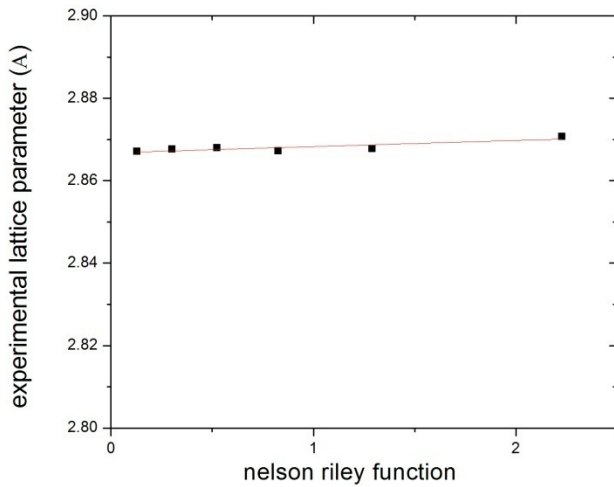
(a)



(b)



(c)



(d)

Fig. 4.8: Nelson Riley extrapolation of data from X-ray diffraction experiment for accurate determination of ferrite lattice parameter in samples(a)G95, (b) EP19, (c) EP20, (d)EP21

This extrapolation if done for ferrite phase in all the samples (fig 4.8) and the result of lattice parameter calculation is tabulated in table 4.3

Table 4.3: Careful look reveals that, lattice parameter of ferrite phase is little higher for EP19 but has decreased in the other two electropulsed samples.

Sample Name	Ferrite Lattice Parameter (nm)
G95	0.28672
EP19	0.28684
EP20	0.28671
EP21	0.28668

4.5.2 Relation to alloying element distribution

Presence and concentration of solute atom directly affects lattice parameter of the alloy [Nagarjuna and Sharma, 1999; Lee and Lee, 2005; Sidot *et al.*, 2005]. In our system silicon and manganese are substitution elements and carbon is interstitial solute. Electropulsing being a microsecond procedure, it is reasonably assuming that there is no diffusion of manganese and silicon atoms in this short duration. This is also evident from the fact that no precipitates have been detected in the micrographs. Carbon being interstitial atom has high diffusivity and its motion causes alteration of local composition, and hence the microscopic structure. The lattice parameter of ferrite phase can be calculated by the following equation when the carbon containment is negligible [Lee and Lee, 2005].

$$a_{\alpha} = 0.28664 + 0.00006 \times \text{Mn} - 0.00003 \times \text{Si} \quad (4.8)$$

where the ferrite lattice parameter a_{α} is in nanometer and concentrations of manganese and silicone are in weight percentage.

This also shows that to have any accuracy over solute measurement, we need to obtain lattice parameter information at least up to five significant digits. This equilibrium lattice parameter is expected to be 0.28666 nm for ferrite, which is a very slight change from pure iron.

Taking into account of carbon concentration in ferrite phase, which can be caused by dissolution of cementite in pearlite under thermo-mechanical processing, lattice parameter is quantified by [Lvet *al.*, 2008].

$$a_{\alpha} = (0.28664 \pm 0.0001) + (0.84 \pm 0.08) \times 10^{-3} \times C_{\alpha} \quad (4.9)$$

Carbon concentration in ferrite phase can be estimated using

$$C_{\alpha} = \Delta a_{\alpha} \frac{10^3}{0.84 \pm 0.08} \text{ at \%} \quad (4.10)$$

These equations are used to estimate average carbon concentration in ferrite phase in different samples before and after electropulsing (table 4.4).

Table 4.4: Estimated carbon concentration in ferrite phase of four samples under observation

Sample Name	Carbon in Ferrite Phase (at %)
G95	0.07±0.01
EP19	0.22±0.02
EP20	0.06±0.01
EP21	0.00±0.01

This shows that electropulsing has increased carbon into ferrite matrix to a unstable level after inadequate electropulsing and excess of which expelled carbon from ferrite and makes cementite particle and the material becomes thermodynamically more stable.

4.5.3 Peak broadening factors and analysis

Light diffraction in polycrystalline does not show peaks of zero thickness vertical lines. They are rather broadened due to imperfections in the crystal and measurement system. One of the basic deviations from assumptions of Bragg's law is that the crystals are not infinite in size. Diffraction occurs at angles near to but not exactly equal to Bragg angle. Superposition of all the very small crystals causes

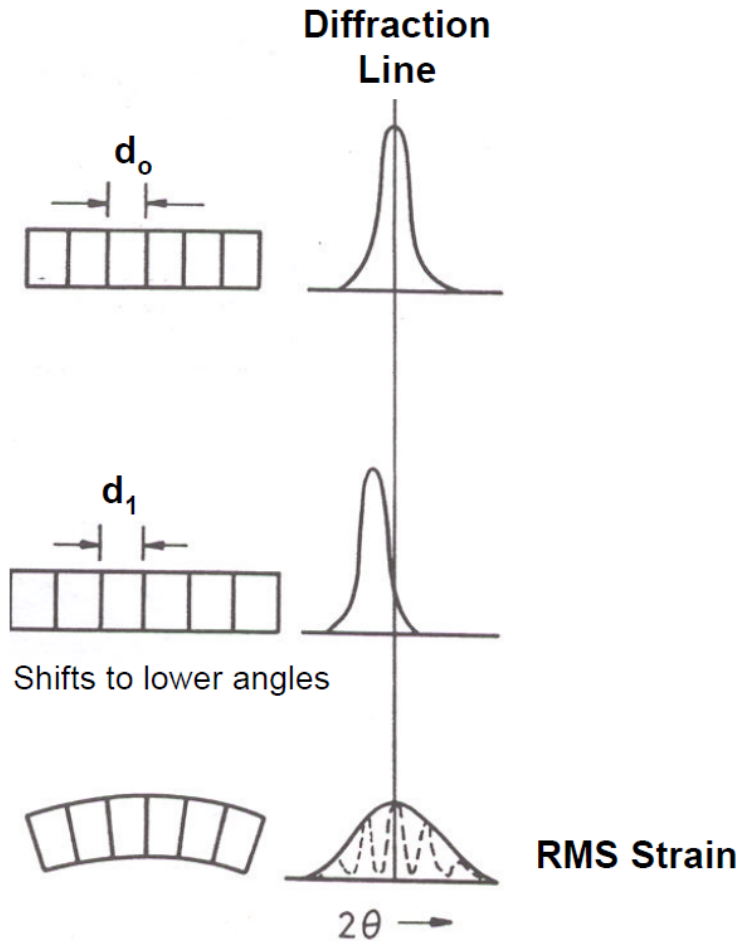
broadening in the pattern. Exact mathematical treatment of this phenomenon gives rise to Scherrer equation.

$$t = \frac{0.9\lambda}{B^x \cos \theta} \quad (4.11)$$

The smaller the grain size, the broader the peaks are in terms of full width at half maxima (FWHM). The crystal size mentioned in this relationship is the average grain size throughout the materials volume.

Similar kind of non-idealness comes from crystal defects due to the aperiodicity involved. This gives rise to micro-stress which is non-uniform in nature over different part within even a single grain. Due to this smaller lower intensity diffractions peaks arises both for compressed and elongated parts covering some region both at the higher than and lower than Bragg angle. All of them together look like a broadened peak in experimental observation (fig 4.9).

The other kind of stress involved in peak modification is macro-stress. The stress is uniform over large range of materials and causes the general change of lattice parameter. The example is the materials under uniform compression. The light diffraction peaks are not broadened in such case but shifted, as demonstrated in fig 4.9. In the present work, the macro-stress is due to the excess containment of carbon.



Exceeds d_0 on top, smaller than d_0 on the bottom

Fig. 4.9: Effects of uniform and non-uniform strain on diffraction peak position and width.

Differentiating Bragg's law with respect to d-spacing, we get the relation between peak broadening and non-uniform strain in the sample.

$$B^x = \Delta 2\theta = -2 \frac{\Delta d}{d} \tan \theta \quad (4.12)$$

This variation of Bragg angle contains both tensile and compressive micro strain. So we need to use half of its numeric value for maximum strain without sign. When multiplied with elastic modulus, this can give the presented maximum micro-stress.

To do this a reference powder diffraction experiment is done under exact same settings in the diffractometer with alumina sample with no strain involved and very large sized crystallites (fig 4.10).

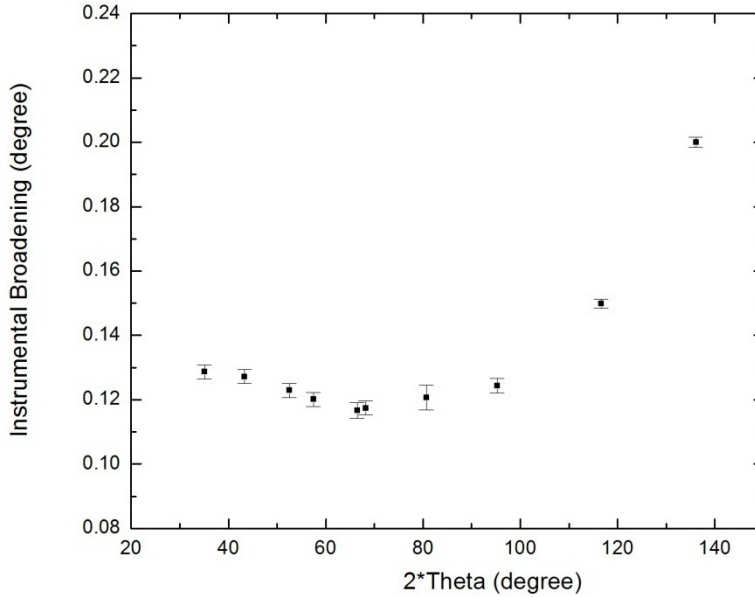


Fig.

4.10: Instrumental broadening as measured with alumina reference crystal

For Lorentzian peaks, broadening due to different causes gets added up and for Gaussian peaks they have a sum of square relation.

$$B_{\text{exp}}^x = B_{\text{size}}^x + B_{\text{strain}}^x + B_{\text{inst}}^x \quad (4.13)$$

$$(B_{\text{exp}}^x)^2 = (B_{\text{size}}^x)^2 + (B_{\text{strain}}^x)^2 + (B_{\text{inst}}^x)^2 \quad (4.14)$$

In this case experimental data follows Lorentzian distribution so the first relation will be used for all data.

Once instrumental broadening is accounted for, size and strain related broadening taken together gives the equation,

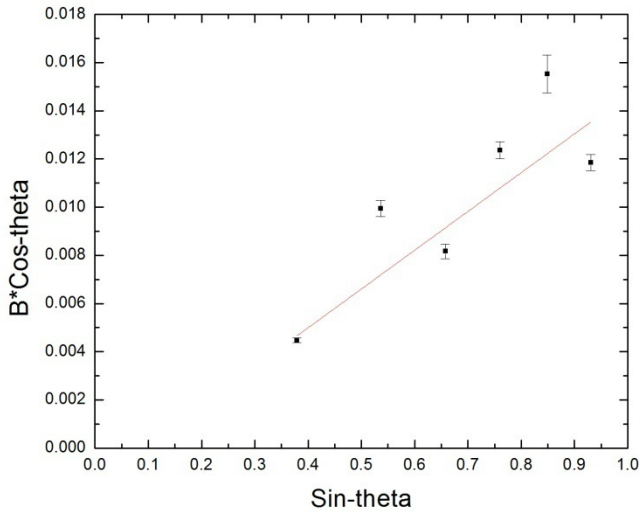
$$B^x = \frac{0.9\lambda}{t \cos \theta} + 2 \frac{\Delta d}{d} \tan \theta \quad (4.15)$$

$$\text{Or, } B^x \cos \theta = \frac{0.9\lambda}{t} + 2 \frac{\Delta d}{d} \sin \theta \quad (4.16)$$

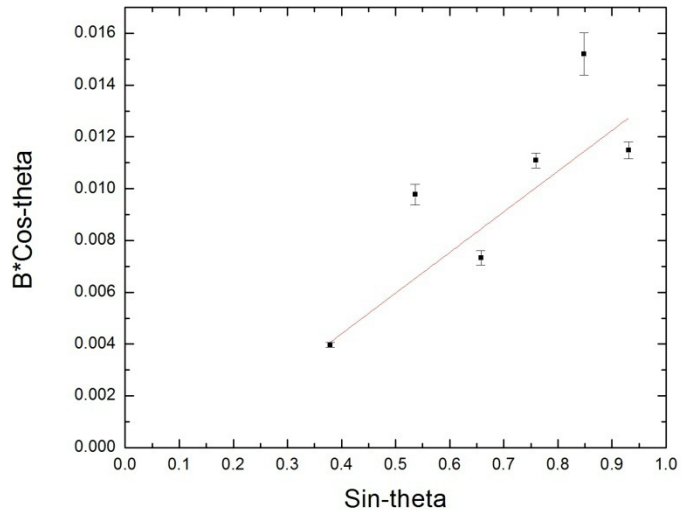
$$\text{Or, } \frac{B^x \cos \theta}{\lambda} = \frac{0.9}{t} + 2 \frac{\Delta d}{d} \frac{\sin \theta}{\lambda} \quad (4.17)$$

So if we plot $B^x \cos \theta$ in y-axis and $\sin \theta$ in x-axis for broadening related data for all peaks of a phase in a sample, we get $y=mx+c$ form of linear plot with $4 \times \text{strain}$ (unsigned) in that particular phase as slope of it and $0.9 \times \text{inverse of grain size} \times \lambda$ as the y-axis intercept. This basic analysis can be used to separate strain and size broadening in diffraction peaks. The strain computer this way is the root mean square of all the strain fields present.

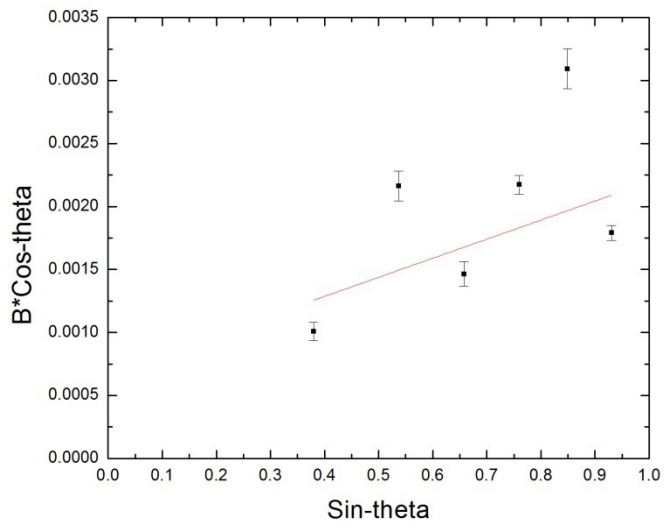
To estimate total experimental broadening, each ferrite peak is fitted into Lorentz function as described before. Broadening and central position of peak is determined from that with appropriate error bar then Williamson Hall plotting is done (Fig 4.11).



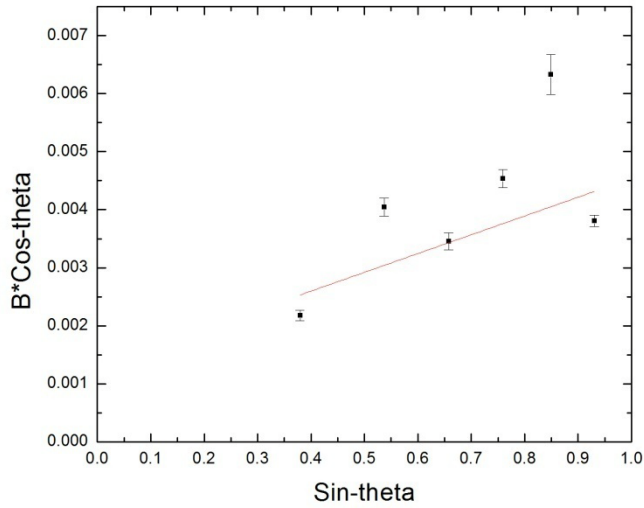
(a)



(b)



(c)



(d)

Fig. 4.11: Williamson Hall plot for ferrite phase in (a) G95 (b) EP19 (c) EP20 (d) EP21 sample

When micro stress level in ferrite phase of all four samples are calculated from Williamson Hall plot, that in G95 and under-electropulsed sample EP19 are close but drastically lower in the higher electropulsed samples as evident from table 4.5

Sample	Micro stress (MPa)
G95	712
EP19	695
EP20	67
EP21	139

Table 4.5: micro-stress level in ferrite phase of different samples as obtained from Williamson Hall analysis

If we consider that this micro stress arises from local shear stress due to dislocations then, dislocation density can be estimated as (48)

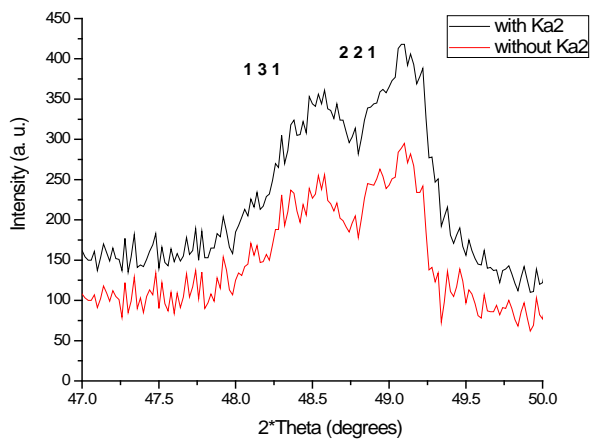
$$\rho_d = \left(\frac{\sigma_{rs}}{0.89 \times \mathbf{b} \times G} \right)^2 \quad (4.18)$$

Taking Burgers vector 0.25 nm, shear modulus of ferrite at 80 GPa rough estimate of dislocation density in ferrite phase is tabulated in table 4.6

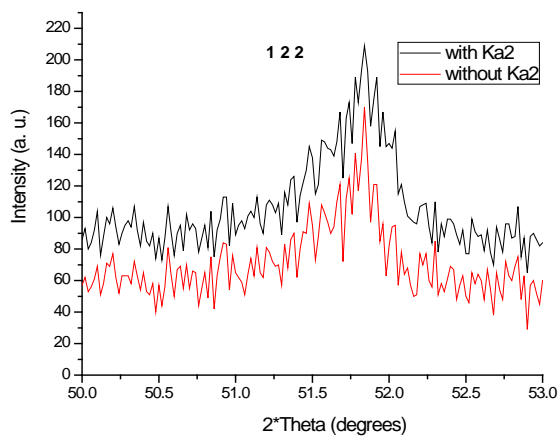
Sample	Dislocation density in ferrite phase
G95	1.66×10^{15}
EP19	1.58×10^{15}
EP20	1.46×10^{13}
EP21	6.3×10^{13}

4.5.4 Cementite peaks

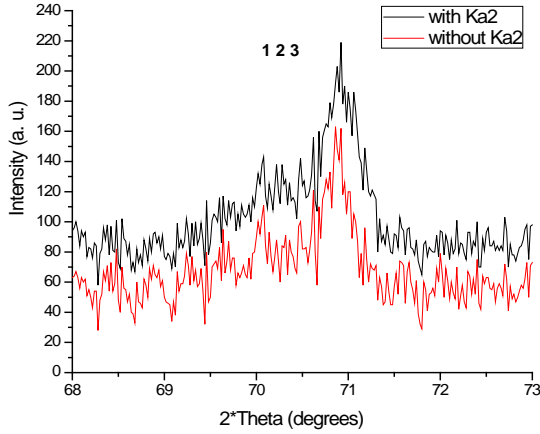
Due to small phase fraction small crystallite effect and heavy deformation of cementite which modifies the internal structure as researched by others [Languillaume *et al.* 1997; Hong *et al.*, 1999; Nam *et al.*, 2000; Sauvage *et al.*, 2000; Hono *et al.*, 2001] it is impossible to detect cementite X-ray diffraction peaks without powerful synchrotron source, in as drawn wire (G95 sample). Same is true for sample EP19, which also supports that no major change happens in EP19 cementite structure. However careful scanning reveals cementite peaks in EP20 (Fig. 4.12) and EP21. Williamson Hall analysis (fig 4.13) of EP20 sample's cementite peaks gives a volume averaged crystallite size of 70 nm and a stress level of 130 MPa (Fig. 4.10). This measured crystallite size supports what is observed in electron microscopy.



(a)



(b)



(c)

Fig. 4.12: diffraction peaks for cementite in EP20 sample for a) (131) plane and (221) plane b) (122) plane and c) (123) plane

4.6 Resistivity measurement

Change of electrical resistivity reflects the alteration of chemical composition, structural changes, phase transition, precipitates and material degradation sensitively [Yu *et al.*, 1999; Nahm *et al.*, 2002; Mohanty and Bhagat, 2003; Park and Lee, 2007]. In the present work, the resistivity was measured by four probe method. It is noticed the resistivity of EP19 is increased in comparison with un-electropulsed sample, but EP20 and EP21 shows increased resistivity than EP19 (Fig. 4.15). These must be due to the electropulse-induced structural transformation such as solute redistribution or phase transitions.

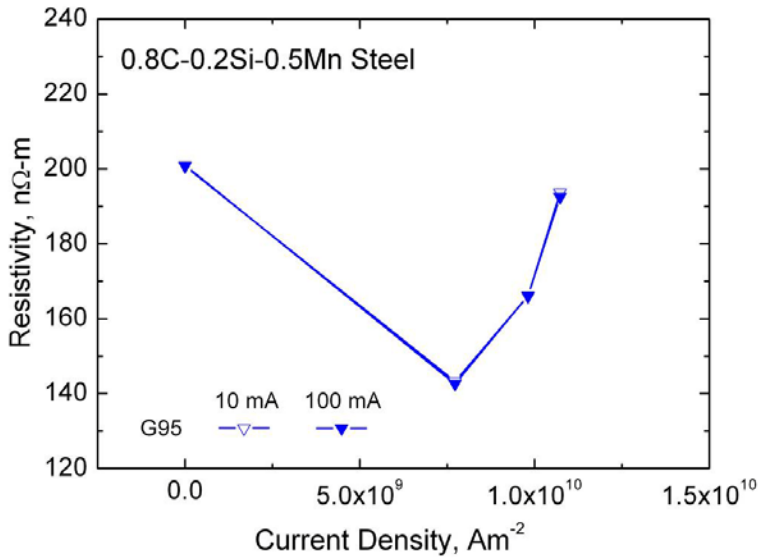


Fig. 4.14: electrical resistivity plot for non-electropulsed and electropulsed samples showing changes for varying levels of pulsing

4.7 Hardness test

It is found that the Vickers hardness is decreasing as the increasing of applied electric current density. The experimental results are given in Table 4.6 and also plotted in Figure 4.16. EP20 and EP21 have much lower hardness value due to spheroidization. Hardness value does indicate the level of spheroidization [Atasoy and Ozbilen, 1989; Obrien and Hosford, 2002].

Sample	Hardness (HV ₁₀)
G95	564
EP19	559
EP20	480
EP21	339

Table 4.6: Hardness values of electropulsed and non electropulsed samples

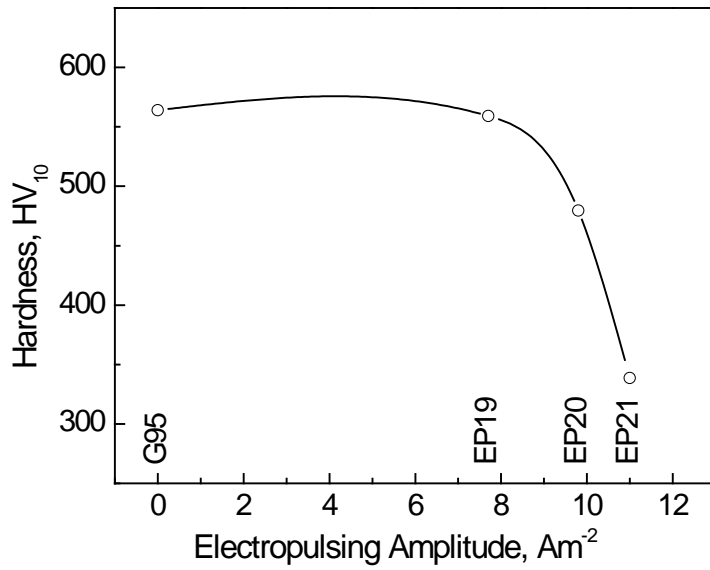


Fig. 4.15: Decreasing pattern in Vickers hardness of different samples measured with 10kg load

Chapter 5

Conclusion

The aim of this study was to understand the effect of electropulsing on pearlitic steel from a fundamental thermodynamic point of view. Previous reports so far were unable to shed light on the underlying reason behind electropulsing enhanced phase transformation. Here a rigorous methodology is built to solve electromagnetics of electropulsing to know the current redistribution due to microstructural and other changes. Then equations are derived to correlate it with change in thermodynamic free energy. Later on simulations using this theory are done for ferrite cementite system, which revealed very interesting phenomena in pearlite under electropulsing condition. It suggested that very high density electropulsing can make the procedure of breaking down cementite plates into very fine particles, thermodynamically favorable, which is otherwise not feasible due to increased surface free energy. Also important conclusion was that, this phenomenon is easier achieved at close to room temperature rather than at an elevated temperature.

Experiments were designed to actually observe this new phenomenon by using very high discharge voltage (higher amplitude of electropulsing) across thin (higher current density) cold drawn (non-equilibrium structure have more chance of moving to equilibrium) pearlite wire. This way, the designed phase transformation occurred at a higher than critical discharge voltage (6 kV). Very fine nanometer scale cementite particles similar in dimension as the starting plate thickness were formed. The whole material had a much lower residual stress level after successful electropulsing. Both in terms of time needed (<1 ms; >7 orders of magnitude faster than spheroidization process) room temperature operation (900K – 1000k for spheroidization) the particle size obtained, the electropulsed microstructure proves a wholly different class of transformation happening.

This whole work shows how it possible to predesign solid phase transformation based structure modification which is impossible to do under normal thermo-mechanical treatment, with the help of electropulsing. Instead of laborious

experiment which is necessary for gathering knowledge how any material will behave under electropulsing, the proposed scheme gives the option of feasibility study of electropulsing based phase transformation in different materials, as simulated and experimentally verified in pearlite system.

References

Alia P., Andreone D., Turtelli R.S., Vinai F. and Rinontino G.: Structural relaxation and irreversible changes of electrical resistivity of Fe-Ni-Mo-B amorphous alloys, *Journal of Applied Physics*, Vol. 53(12), pp. 8798-8804, 1982

Atasoy O.E. and Ozbilen S.: Pearlite Spheroidization, *Journal of Materials Science*, Vol. 24, pp. 281-287, 1989

Barghout J.Y., Lorimer G.W., Pilkington R. and Prangnell P.B.: The effects of second phase particles. Dislocation density and grain boundaries on the electrical conductivity of aluminum alloys, *Material Science Forum*, Vol. 217-222, pp. 975-980, 1996

Barnak J.P., Sprecher A.F. and Conrad H.: Colony size reduction in eutectic Pb-Sn casting in electropulsing, *Scripta Metallurgica et Materialia*, Vol. 32(6), pp. 879-884, 1995

Campbell J. and Conrad H.: Influence of electric current on the quench aging of a low carbon steel, *Scripta Metallurgica et Materialia*, Vol. 31(1), pp. 69-74, 1994

Cao W.D., Lu X.P., Sprecher A.F. and Conrad H.: Increased hardenability of steel by an external electric field, *Materials Letters*, Vol. 9(5.6), pp. 193-197, 1990

Cao W.D., Sprecher A.F. and Conrad H.: Effect of strain rate on electroplastic effect in Nb, *Scripta Metallurgica* Vol. 23, pp. 151-155, 1989

Chattopadhyay S. and Sellars C.M.: Quantitative measurement of pearlite spheroidization, *Metallography*, Vol. 10, pp. 89-105, 1977

Chattopadhyay S. and Sellars C.M.: Kinetics of pearlite spheroidization during static annealing and during hot deformation, *Acta Metallurgica*, Vol. 30, pp. 157-

170, 1982

Conrad H., Cao W.D., Lu S.P. and Sprecher A.F.: Effect of electric field on cavitation in superplastic aluminum alloy 7475, *Materials Science and Engineering A*, Vol.138, pp. 247-258, 1991

Conrad H., Cao W.D., Lu S.P. and Sprecher A.F.: Effect of electric field on superplasticity of 7475 Al, *Scripta Metallurgica* Vol. 23, pp. 821-824, 1989

Conrad H., Guo Z. and Sprecher A.F.: Effect of an electric field on recovery and recrystallization of Al and Cu, *Scripta Metallurgica* Vol. 23, pp. 697-702, 1989

Conrad H., Guo Z. and Sprecher A.F.: Effect of electropulse duration and frequency on grain growth in Cu, *Scripta Metallurgica et Materialia* Vol. 24, pp. 359-362, 1990

Conrad H., Karam N. and Mannan S.: Effect of electric current pulses on the recrystallization of copper, *Scripta Metallurgica* Vol. 17, pp. 411-416, 1983

Conrad H., Karam N. and Mannan S.: Effect of prior cold work on the influence of electric current pulses on the recrystallization of copper, *Scripta Metallurgica* Vol. 18, pp. 275-280, 1984

Conrad H., Karam N., Mannan S. and Sprecher A.F.: Effect of electric current pulses on the recrystallization kinetics of copper, *Scripta Metallurgica* Vol. 22, pp. 235-238, 1988

Cullity B.D. and Stock S.R.: 2001, *Elements of X-ray diffraction*, 3rd Ed. Prentice Hall

Dexter D.L.: Scattering of electrons in metals by dislocation, Vol. 86(5), pp. 770-774, 1952

Ding F., Tang G., Xu Z. and Tian S.: A New Method for Improving Strength and Plasticity of Steel Wire, *Journal of Materials Sciences and Technology*, Vol. 23(02),

pp. 273-276, 2007

Du X.N., Yin S.M., Liu S.C., Wang B.Q. and Guo J.D.: Effect of the electropulsing on mechanical properties and microstructure of an ECAPed AZ31 Mg alloy, *Journal of Material Research*, Vol. 23(6), pp. 1570-1577, 2008

Hong M.H., Reynolds W.T., Tarui T. and Hono K.: Atom Probe and Transmission Electron Microscopy Investigations of Heavily Drawn Pearlitic Steel Wire, *Metallurgical and Materials Transaction A*, Vol. 30A, pp. 717-727, 1999

Hono K., Ohnuma M, Murayama M., Nishida S., Yoshie A. and Takahashi T.: Cementite decomposition in heavily drawn pearlitic steel wire, *ScriptaMaterialia*, Vol. 44, pp. 977-983, 2001

Kelton K.F. and Spaepen F.: Kinetics of structural relaxation in several metallic glasses observed by changes in electrical resistivity, *Physical Review B*, Vol. 30(10), pp. 5516-5524, 1984

Kiryanchev N.E., Troitskii O.A., Krasnoyarskii V.V., Petrova L.M., Stashenko V.I., Gavrish A.A. and Miseev V.P.: Electroplastic Drawing of Trip Steel, *Elektronnaya Obrabotka Materialov*, Issue 2, pp. 54-58, 1985

Languillaume J., Kapelski G. and Baudelet B.: Cementite dissolution in heavily cold drawn pearlitic steel wires, *ActaMaterialia*, Vol. 45(3), pp. 1201-1212, 1997

Lee S.J. and Lee Y.K.: Quantitative analyses of ferrite lattice parameter and solute Nb content in low carbon microalloyed steels, *ScriptaMaterialia*, Vol. 52, pp. 973-976, 2005

Li S. and Conrad H.: Electric field strengthening during superplastic creep of Zn-5wt% Al: a negative electroplastic effect, *ScriptaMaterialia*, Vol. 39(7), pp. 847-851, 1998

Li Q.C., Li R.X., Chang G.W. and Zhai Q.J.: Research of microstructure of

spherical graphite iron by

electropulsing annealing, *Journal of Materials Sciences and Technology*, Vol. 209(4), pp. 2015-2020, 2009

Livesey S.J., Duan X., Priestner R. and Collins J.: An electroplastic effect in 31/4% silicon steel, *ScriptaMaterialia*, Vol.44, pp. 803-809, 2001

Lv Z.Q., Jiang P., Wang Z.H., Zhang W.H., Sun S.H. and Fu W.T.: XRD analyses on dissolution behavior of cementite in eutectoid pearlitic steel during cold rolling, *Materials Letters*, Vol. 62, pp. 2825-2827, 2008

Mohanty A.N. and Bhagat O.N: Electrical resistivity and phase transformations in steel, *Materialwissenschaft und Werkstofftechnik*, Vol. 34(1), pp. 96-101, 2003

Moiseenko M.M. and Troitskii O.A.: Electroplastic deformation of lead cadmium and zinc crystals, *Russian Metallurgy (Metally)*, Issue 1, pp. 159-161, 1987

Nagarjuna S. and Sharma D.S.: On the variation of lattice parameter of Cu solid solution with solute content in Cu-Ti alloys, *ScriptaMaterialia*, Vol. 41(4), pp. 359-363, 1999

Nahm S.H., Kim Y.I., Yu K.M. and Kim A.: Evaluation of fracture toughness of degraded Cr-Mo-V steel using electrical resistivity, *Journal of Materials Science*, Vol. 37, pp. 3549-3553, 2002

Nam W.J., Bae C.M., Oh S.J. and Kwon S.J.: Effect of interlamellar spacing on cementite dissolution during wire drawing of pearlitic steel wires, *ScriptaMaterialia*, Vol. 42, pp. 457-463, 2000

O'Brien J.M. and Hosford W.F.: Spheroidization cycles for medium carbon steels, *Metallurgical and Materials transaction A*, Vol. 33A, pp. 1255-1261, 2002

Park J.S. and Lee Y.K.: Determination of Nb(C,N) dissolution temperature by

electrical resistivity measurement in a low-carbon microalloyed steel, *ScriptaMaterialia*, Vol. 56, pp. 225-228, 2007

Qin R. and Su S.: Thermodynamics of crack healing under electropulsing, *Journal of Material Research*, Vol. 17(8), pp. 2048-2052, 2002

Qin R., Su S.X., Guo J.D., He G.H. and Zhou B.L.: Suspension effect of nanocrystalline grain growth under electropulsing, *Nanostructured Materials*, Vol. 10(1), pp. 71-76, 1998

Qin R.S. and Zhou B.L.: Effect of electric current pulses on grain size in casting, *International Journal of Nonequilibrium Processing*, Vol. 11, pp. 77-86, 1998

Sauvage X., Copreaux J., Danoix F. and Blavette D.: Atomic-scale observation and modelling of cementite dissolution in heavily deformed pearlitic steels, *Philosophical Magazine A*, Vol. 80(4), 781-796, 2000

Sidot E., Kahn-Harari A., Cesari E. and Robbiola L.: The lattice parameter of α -bronzes as a function of solute content: application to archaeological materials, *Materials science and Engineering A*, Vol. 393, pp. 147-156, 2005

Sosnin A.V., Gromova A.V., Suchkova E.Y., Kozlov E.V., Ivanov Y.F. and Gromov V.E.: The structural-phase state changes under the pulse current influence on the fatigue loaded steel, *International Journal of Fatigue*, Vol. 27, pp.1221-1226, 2005

Tang G., Zhang J., Yang Y., Zhou H. and Fang W.: The engineering application of the electroplastic effect in the cold-drawing of stainless steel wire, *Journal of Material Processing Technology*, Vol. 137, pp. 96-99, 2003

Tang G., Zhang J., Zheng M., Zhang J., Fang W. and Li Q.: Experimental study of electroplastic effect on stainless steel wire 304L, *Materials Science and Engineering A*, Vol. 281, 263-267, 2000

Tang G., Zheng M., Zhu Y., Zhang J., Fang W. and Li Q.: The application of the

electro-plastic technique in the cold-drawing of steel wires, Journal of Materials processing technology, Vol. 84, pp. 268-270, 1998

Thompson S.M. and Tanner B.K.: The magnetic properties of specially prepared pearlitic steels of varying carbon content as a function of plastic deformation, Journal of Magnetism and Magnetic Materials, Vol. 132, pp. 71-88, 1994

Troitskii O.A.: Electron plastic effect in metals, ProblemyProchnosti, Issue 2, pp. 176, 1984

Troitskii O.A.: Problem of the effect of electrical pulses on the process of drawing thin metal wires, Russian Metallurgy (Metally), Issue 2, pp. 192-195, 1984

Troitskii O.A. and Moiseenko M.M.: Action of series of electric pulses on deformation of zinc crystals, Russian Metallurgy (Metally), Issue 6, pp. 148-151, 1985

Troitskii O.A., Savenko V.S., Stashenko V.I., Shorop G.N., Kiryanchev N.E., Kalosha V.K., Opimakh V.N. and Kalymbetov P.U.: Multistage electroplastic drawing of copper wire, Issue 5, pp. 96-98, 1986

Wang X.L., Guo J.D., Wang Y.M., Wu X.Y. and Wang B.Q.: Segregation of lead in Cu-Zn alloy under electric current pulses, Applied Physics Letters, Vol. 89, 061910, 2006

Xiao S.H., Guo J.D. and Li S.X.: The effect of electropulsing on dislocation structures in [233] coplanar double-slip-oriented fatigued copper single crystals, Philosophical Magazine Letters, Vol. 82(11), pp. 617-622, 2002

Xiao S.H., Guo J.D., Wu S.D., He G.H. and Li S.X.: Recrystallization in fatigued copper single crystals under electropulsing, Scripta Materialia Vol. 46, pp. 1-6, 2002

Yang D. and Conrad H.: Exploratory study into the effects of an electric field and of high current density electropulsing on the plastic deformation of TiAl,

Intermetallics, Vol. 9, pp. 943-947, 2001

Yao K.F., Wang J., Zheng M., Yu P. and Zhang H.: A research in electroplastic effects in wire drawing process of an austenitic stainless steel, *ScriptaMaterialia* Vol. 45, pp. 533-539, 2001

Yao K.F., Yu P., Wang J., Fang W. and Zheng M.X.: Effect of high density current pulses on work hardening behaviours of austenitic stainless steel in wire drawing deformation, *ActaMetallurgicaSinica*, Vol 14(5), pp. 341-346, 2001

Yu K.M., Nahm S.H. and Kim Y.I.: Toughness degradation evaluation of 1Cr–1Mo–0.25V steel by electrical resistivity, *Journal of Materials Science Letters*, Vol. 18, pp. 1175-1176, 1999

Zelin M.: Microstructure evolution in pearlitic steels during wire drawing, *ActaMaterialia*, Vol. 50, pp. 4431-4447, 2002

Zhang W., Sui M.L., Hu K.Y., Li D.X., Guo X.N., He G.H. and Zhou B.L.: Formation of nanophases in a Cu–Zn alloy under high current density electropulsing, *Journal of Material Research*, Vol. 15(10), pp. 65-68, 2000

Zhang W., Zhou Y.Z., Sui M.L., He G.H., Guo J.D. and Li D.X.: Formation of nanoscale α -Al in a superdralumin under high current density electropulsing, *Journal of Material Science Letters*, Vol. 21, pp. 1923-1925, 2002

Zhou Y., Qiao D., He G. and Guo J.: Improvement of mechanical properties in a saw blade by electropulsing treatment, *Material Letters*, Vol. 57, pp. 1566– 1570, 2003

Zhou Y., Guo J., Gao M. and He G.: Crack healing in a steel by using electropulsing technique, *Material Letters*, Vol. 58, pp. 1732– 1736, 2004

Zhou Y., Guo J., Zhang W. and He G.: Influence of electropulsing on nucleation during phase transformation, *Journal of Material Research*, Vol. 17(12), pp. 3012-

3014, 2002

Zhou Y., Zeng Y., He G. and Zhou B.: The healing of quenched crack in 1045 steel under electropulsing, *Journal of Material Research*, Vol. 16(1), pp. 17-19, 2001

Zhou Y.Z., Zhang W., Guo J. and He G.: Diffusive phase transformation in a Cu-Zn alloy under rapid heating by electropulsing, *Philosophical Magazine Letters*, Vol. 84(15), pp. 341-348, 2004

Zhou Y., Zhang W., Sui M., Li D., He G. and Guo J.: Formation of a nanostructure in a low-carbon steel under high current density electropulsing, *Journal of Material Research*, Vol. 17(5), pp. 921-924, 2002

Zhou Y., Zhang W., Wang B. and Guo J.: Ultrafine-grained microstructure in a Cu-Zn alloy produced by electropulsing treatment, *Journal of Material Research*, Vol. 18(8), pp. 1991-1997, 2003

Zhou Y., Zhang W., Wang B., He G. and Guo J.: Grain refinement and formation of ultrafine-grained microstructure in a low-carbon steel under electropulsing, *Journal of Material Research*, Vol. 17(8), pp. 2005-2011, 2002

Zhou Y., Xiao S.H. and Guo J.D.: Recrystallized microstructure in cold worked brass produced by electropulsing treatment, *Materials Letters* Vol. 58, pp. 1948-1951, 2004

Acknowledgement

I want to express my gratitude to my supervisors, Prof. Bhadeshia H.K.D.B. and Prof. Qin Rongshan for their encouragement guidance and support. Prof. Bhadeshia has taught me how to be objective while doing science. Many hours I have spent with Prof. Qin discussing even about personal problems beside research. The philosophies that I have learnt from him will be leading me in the future both in scientific adventures and in life outside it.

I am grateful to Prof. Kim In Gee and Prof. Suh Dong Woo for their friendliness, helping nature and all the good advice that I have got from them. I would like to express my heartfelt thanks to all members in Computational Metallurgy Laboratory, for all their help during my 2 year stay in Korea. Especially without Isaac, I may not have been able to finish the experimental part of this work. Last but the most important peoples in my life, my parents, with their everlasting love and encouragement for higher studies have helped me put myself where I am now.